
Halo Concentration, Galaxy Red Fraction, and Gas Properties of Optically-defined Merging Clusters *

Nobuhiro OKABE^{1,2,3}, Masamune OGURI^{4,5,6}, Hiroki AKAMATSU⁷, Akinari HAMABATA⁵, Atsushi J. NISHIZAWA⁸, Elinor MEDEZINSKI⁹, Yusei KOYAMA^{10,11}, Masao HAYASHI¹², Taizo OKABE⁵, Shutaro UEDA¹³, Ikuyuki MITSUISHI¹⁴ and Naomi OTA¹⁵

¹Department of Physical Science, Hiroshima University, 1-3-1 Kagamiyama, Higashi-Hiroshima, Hiroshima 739-8526, Japan

²Hiroshima Astrophysical Science Center, Hiroshima University, 1-3-1 Kagamiyama, Higashi-Hiroshima, Hiroshima 739-8526, Japan

³Core Research for Energetic Universe, Hiroshima University, 1-3-1, Kagamiyama, Higashi-Hiroshima, Hiroshima 739-8526, Japan

⁴Research Center for the Early Universe, University of Tokyo, Tokyo 113-0033, Japan

⁵Department of Physics, University of Tokyo, Tokyo 113-0033, Japan

⁶Kavli Institute for the Physics and Mathematics of the Universe (Kavli IPMU, WPI), University of Tokyo, Chiba 277-8582, Japan

⁷SRON Netherlands Institute for Space Research, Sorbonnelaan 2, 3584 CA Utrecht, The Netherlands

⁸Institute for Advanced Research, Nagoya University Furocho, Chikusa-ku, Nagoya, 464-8602 Japan

⁹Department of Astrophysical Sciences, Princeton University, Princeton, NJ 08544, USA

¹⁰Subaru Telescope, National Astronomical Observatory of Japan, National Institutes of Natural Sciences, 650 North A'ohoku Place, Hilo, HI 96720, USA

¹¹Graduate University for Advanced Studies (SOKENDAI), Osawa 2-21-1, Mitaka, Tokyo 181-8588, Japan

¹²National Astronomical Observatory of Japan, Osawa 2-21-1, Mitaka, Tokyo 181-8588, Japan

¹³Institute of Astronomy and Astrophysics, Academia Sinica, P.O. Box 23-141, Taipei 10617, Taiwan

¹⁴Department of Physics, Nagoya University, Aichi 464-8602, Japan

¹⁵Department of Physics, Nara Women's University, Kitauoyanishi-machi, Nara, Nara 630-8506, Japan

*E-mail: okabe@hiroshima-u.ac.jp

Received ; Accepted

Abstract

We present multi-wavelength studies of optically-defined merging clusters, based on the Hyper Suprime-Cam Subaru Strategic Program. Luminous red galaxies, tracing cluster mass distributions, enable to identify cluster subhalos at various merging stages, and thus make a homogeneous sample of cluster mergers, which is unbiased with respect to the merger boost of the intracluster medium (ICM). We define, using a peak-finding method, merging clusters with multiple-peaks and single clusters with single-peaks from the CAMIRA cluster catalog. Stacked

weak-lensing analysis indicates that our sample of the merging clusters is categorized into major mergers. The average halo concentration for the merging clusters is $\sim 70\%$ smaller than that of the single-peak clusters, which agrees well with predictions of numerical simulations. The spatial distribution of subhalos is less centrally concentrated than the mass distribution of the main halo. The fractions of red galaxies in the merging clusters are not higher than those of the single-peak clusters. We find a signature of the merger boost of the ICM from stacked *Planck* Sunyaev-Zeldovich effect and *ROSAT* X-ray luminosity, but not in optical richness. The stacked X-ray surface brightness distribution, aligned with the main-subhalo pairs of low redshift and massive clusters, shows that the central gas core is elongated along the merger axis and overall gas distribution is misaligned by ~ 60 deg. The homogeneous, unbiased sample of cluster mergers and multi-wavelength follow-up studies provide a unique opportunity to make a complete picture of merger physics over the whole process.

Key words: Galaxies: clusters: intracluster medium - X-rays: galaxies: clusters - Gravitational lensing: weak - Galaxies: stellar content

1 Introduction

Based on hierarchical structure formation scenario of the Cold Dark Matter (CDM) paradigm, small structures form first, which grow into more massive objects through matter accretion along their surrounding filamentary structure. Galaxy clusters sometimes merge with less massive clusters, groups, and galaxies. Minor mergers with a mass ratio < 0.1 are ubiquitous, whereas major mergers with similar-mass are an intermittent event. Even so, various gas phenomena are induced by major mergers, specifically merger shocks and turbulence, which gives a significant impact on both the thermal history and cluster evolution (e.g. Takizawa & Naito 2000; Ricker & Sarazin 2001; Sarazin 2002; ZuHone 2011). The merging process can be broadly divided into three phases; pre-merger (or early phase), on-going, and post-merger. The early phase of cluster mergers is the phase before the two cluster cores start to interact with each other. No significant effect on the intracluster medium (ICM) is appeared. On-going merger is the phase when the two cores are passing through. The close interaction triggers merger shocks, resulting in heating the temperature of the ICM and increasing the X-ray luminosity of clusters. The increase of the temperature and X-ray luminosity last on about half of the sound crossing time, less than a few Gyrs (e.g. Ricker & Sarazin 2001). The feature is well-known as “*merger boost*”, giving rise to a significant effect on cluster cosmology (e.g. Krause et al. 2012; Kay et al. 2012; Yu et al. 2015). At the post merger phase after cluster passages, gas temperature and X-ray luminosity decrease because of adiabatic expansion. In some cases, they become below the initial quantities and regarded as X-ray underluminous clusters.

During cluster mergers, the physical state of merging clusters is instantly and dramatically deviated from virialization.

Furthermore, the merger-induced shocks and turbulence generate relativistic particles, and diffuse radio emission, so-called radio relics and halos, are observed in various merging clusters (e.g. Govoni et al. 2004; van Weeren et al. 2010; Feretti et al. 2012), although the physics of particle acceleration has not yet been fully understood (e.g. Fujita et al. 2003; Brunetti et al. 2008; Fujita et al. 2015; van Weeren et al. 2017; Akamatsu et al. 2017). It is therefore of critical importance to understand the microphysical processes underlying cluster mergers and these impacts on cosmological applications.

Our understanding of gas physics in merging clusters, by X-ray and radio observations, is limited in the context of the whole process of cluster mergers. This is because most of observing targets were chosen from X-ray luminous clusters. Since X-ray luminosity is non-linearly increased at on-going phase, we now face to a serious issue of a selection bias toward on-going phase. Indeed, most of well-known merging clusters are at the on-going phase, and X-ray observations of early-/late-phase merging clusters are very limited (e.g. Belsole et al. 2004; Owers et al. 2013; Akamatsu et al. 2016). Hence, a next study of merging clusters is demanded to add new insights into the pool of knowledge on cluster mergers over the whole process including the pre- and post-merger phase. For this purpose, it is of vital importance to define a homogeneous merging cluster sample with a selection function independent of the merger boost of the ICM.

The total mass distribution of galaxy clusters is also affected by cluster mergers. For instance, the concentration parameter, which represents the degree of the concentration of the interior mass density, becomes lower due to the presence of massive subhalos at some distance (e.g. Neto et al. 2007; Duffy et al. 2008; Bhattacharya et al. 2013; Child et al. 2018). Recent weak gravitational lensing studies (e.g. Oguri et al. 2012; Okabe et al. 2013; Umetsu et al. 2014; Merten et al. 2015; Okabe & Smith

* Based on data collected at Subaru Telescope, which is operated by the National Astronomical Observatory of Japan.

2016; Cibirka et al. 2017; Miyazaki et al. 2018a) revealed that the average concentration parameter as a function of cluster masses is in an excellent agreement with predictions of numerical simulations (e.g. Bhattacharya et al. 2013; Meneghetti et al. 2014; Ludlow et al. 2014; Diemer & Kravtsov 2015; Child et al. 2018; Ragagnin et al. 2018). The relation between mass and concentration holds for X-ray selected and shear-selected clusters. However, it has not yet been explored by weak-lensing studies how much the concentration parameter is changed by cluster mergers, because the number of merging clusters was insufficient for detailed studies. Therefore, we need a large sample of merging clusters for weak-lensing analysis.

Several theoretical work discussed how the star formation activity is enhanced by cluster mergers (e.g. Dressler & Gunn 1983; Lavery & Henry 1988; Evrard 1991; Fujita et al. 1999; Bekki 1999; Kapferer et al. 2006; Kronberger et al. 2008). One of the key processes is that a tenuous, hot gas in infalling galaxies is compressed by the ram-pressure or shock fronts of the ICM, and triggers a one-time star-burst. Subsequently, continuous gas stripping in galaxies quenches the star formation during cluster collisions. Since the duration of the star-burst is order of Gyr or less, it is difficult to witness the overall, rapid evolution of star formation and quenching activities. Recent spectroscopic observations of on-going mergers at $z \lesssim 0.4$ (e.g. Stroe et al. 2015, 2017; Deshev et al. 2017) have shown both high and low star formation rates. A large sample of clusters with various merging stages provides a straightforward means of overcoming the relatively large intrinsic scatter of star formation rates.

In short, a construction of a large sample of merging clusters comprising various merging stages provides us with a unique opportunity for follow-up multi-wavelength observations, which will open-up a statistical approach to conduct a more comprehensive study of cluster mergers from the early to late phase. The advantages of the approach are to

- fill in the parameter spaces of cluster mergers, such as merging stages and mass ratios,
- characterize the impact of merging phenomena on the cluster evolution via a phase-separated “anatomy”,
- control the systematics of outliers in scaling relations and construct better mass proxy calibration for cluster cosmology study,
- take a snapshot of various stages of transient phenomena such as shock heating, adiabatic expansion, star formation, quenching process, and particle acceleration.

This kind catalog would be timely in incoming new era of cluster studies based on big data.

The galaxy distribution contains a unique and ideal information to construct a homogeneous, unbiased sample of cluster mergers, thanks to the following five reasons. First, the number of luminous red galaxies is almost conserved during cluster mergers, in contrast to the ICM merger boost. Second, spectro-

scopic observations of all member galaxies in thousands clusters are not realistic, and photometric information is more efficient to search cluster subhalos. Third, the lifetime of galaxy substructure is much larger than that of the collisional gas (e.g. Tormen et al. 2004). Thus, galaxy subhalos survive even after the core passage and can be easily identified at any merging phases. Fourth, the angular resolution of weak-lensing mass reconstruction is too poor to search cluster substructures in normal and small clusters at wide redshift ranges at $0.1 < z < 1.1$ (e.g. Okabe et al. 2014). Furthermore, it suffers from misidentification of background and/or foreground objects accidentally superposed with the targeting clusters. Fifth, as reported in previous studies (e.g. Okabe & Umetsu 2008), the galaxy distribution of luminous red galaxies is very similar to the dark matter distribution of targeting clusters regardless of dynamical states. Thus the galaxy distribution provides a powerful means of identifying cluster mergers. There are, however, two disadvantages of this approach. First, from the photometric information alone it is hard to distinguish between internal subhalos and surrounding halos because of the degeneracy of peculiar velocity and physical separation along the line-of-sight. Second, the galaxy distribution cannot identify dynamical states of cluster mergers, that is, the state of being either before or after the core passage. Therefore, multi-wavelength follow-up studies, especially for individual clusters, are essential for understanding physical properties of defined merging subsamples. The morphology of the ICM which is a compressible fluid provides us with helpful information to distinguish between pre- and post- mergers.

In this paper, we present multi-wavelength studies for optically-defined merging clusters, based on the Hyper Suprime-Cam Subaru Strategic Program (HSC-SSP; Aihara et al. 2018a, 2018b; Miyazaki et al. 2018b; Komiyama et al. 2018; Kawanomoto et al. 2018; Furusawa et al. 2018; Bosch et al. 2018; Huang et al. 2018; Coupon et al. 2018). The HSC-Survey is an ongoing wide-field imaging survey using the HSC (Miyazaki et al. 2015, 2018c) which is a new prime focus camera on the 8.2m-aperture Subaru Telescope. The HSC-SSP survey is composed of three layers of different depths (Wide, Deep and UltraDeep). The Wide layer is designed to obtain five-band (*grizy*) imaging over 1400 deg². The HSC-SSP survey has both excellent imaging quality ($\sim 0.''7$ seeing in *i*-band) and deep observations ($r \lesssim 26$ AB mag). Recently Oguri et al. (2018) constructed a CAMIRA cluster catalog from HSC-SSP S16A dataset covering ~ 240 deg² using the CAMIRA algorithm (Oguri 2014) which is a red-sequence cluster finder based on the stellar population synthesis model fitting. The catalog contains ~ 1900 clusters at $0.1 < z < 1.1$ with richness larger than $N_{\text{cor}} = 15$. Photometric redshifts of the clusters are shown to be accurate at $\sigma_z/(1+z) \sim 0.01$ for the whole redshift range, which are estimated by comparing the photometric redshifts to spectroscopic redshifts of brightest cluster galaxies (BCGs).

We construct a catalog of merging cluster candidates from the CAMIRA cluster catalogue (Oguri et al. 2018). We carry out multi-wavelength studies for the catalog, compiling multi-band dataset from the HSC-SSP photometry (Aihara et al. 2018a; Tanaka et al. 2018) and weak-lensing (Mandelbaum et al. 2018), Sloan Digital Sky Survey (SDSS) spectroscopic data (Abolfathi et al. 2018), *ROSAT* X-ray (Truemper 1982), *Planck* Sunyaev-Zeldovich effect (SZE; Planck Collaboration et al. 2016), the NRAO VLA Sky Survey (NVSS; Condon et al. 1998), and the TIFR GMRT Sky Survey (TGSS; Intema et al. 2017). As a first demonstration of the power of optically-defined subsamples, we in this paper focus on stacking analyses of multi-wavelength dataset. We describe our optical-selected merging clusters and multi-wavelength analyses in Sec. 2. The main results and discussion are presented in Sec. 3. We summarize our results in Sec. 4. Throughout the paper we assume a flat Λ CDM cosmology with $H_0 = 70 \text{ km s}^{-1} \text{ Mpc}^{-1}$, $\Omega_{m,0} = 0.28$ and $\Omega_\Lambda = 0.72$.

2 Data Analysis

2.1 Definition of subsamples

We identify, using a peak-finding method, merging cluster candidates from the CAMIRA cluster catalogue (Oguri et al. 2018) constructed from the HSC-SSP Survey (Aihara et al. 2018a, 2018b; Miyazaki et al. 2018c). We use the HSC-SSP S16A data (Aihara et al. 2018a; Tanaka et al. 2018; Mandelbaum et al. 2018).

We select red-sequence galaxies in color-magnitude plane following Nishizawa et al. (2018). The band combinations are $g-r$, $r-i$, and $i-y$ in the redshift ranges of $0.1 < z < 0.4$, $0.4 < z < 0.7$, and $0.7 < z < 1.1$, in order to cover the 4000\AA break at these redshifts, respectively. The median and width of colors of red-sequence galaxies are the same as Nishizawa et al. (2018). We use red-sequence galaxies of which apparent z -band magnitudes are brighter than the observer-frame magnitude with the constant z -band absolute magnitude $M_z = -18$ ABmag. We also apply the apparent magnitude cut $m_z < 25.5$. We here adopt K-correction in conversion between apparent and absolute magnitudes taking into account passive evolution (Nishizawa et al. 2018). We then construct Gaussian smoothed maps (FWHM = $200h_{70}^{-1}$ kpc) of number densities of red-sequence galaxies within each box size of $1.5r_{200m}$ centered on the CAMIRA positions. In order to avoid photometric outliers in the survey catalog, we do not use luminosity densities which can be significantly affected by these outliers. Here, r_{200m} denotes the radius within which the mean density is 200 times the mean mass density of the Universe at the cluster redshift. To estimate r_{200m} , We assume a scaling relation between the richness, N_{cor} , and the mass, $M_{200m} = 10^{14} h^{-1} (N_{\text{cor}}/15) M_\odot$, because Oguri et al. (2018) have found that richness $N_{\text{cor}} = 15$

roughly corresponds to $M_{200m} = 10^{14} h^{-1} M_\odot$ by a comparison between the observed cluster abundance and the expected halo of Tinker et al. (2008). The r_{200m} spans from $\sim 1h_{70}^{-1}$ Mpc to $\sim 2h_{70}^{-1}$ Mpc. Therefore, with the assumed FWHM of the Gaussian smoothing we can resolve galaxy concentrations with one-tenth or one-twentieth of cluster sizes.

We define the threshold of peak-identifications in the smoothed number density map based on solely by observational data, because both the number of red galaxies and angular sizes of smoothing scale depend on cluster redshifts. It also has the advantage of avoiding the assumption of baryonic physics input in numerical simulations. We use an average of stacked galaxy map at each cluster redshift as the threshold of peak heights. The average peak heights appeared in the stacked maps at a slice of $\Delta z = 0.05$ smoothly change as a function of redshifts, and correspond to 5 galaxies at $z \lesssim 0.8$. We interpolate the average peak heights as a function of cluster redshifts.

Our peak-finding algorithm is composed of three steps. We first identify peaks above the redshift-dependent threshold. Second, we subtract a component of extended galaxy distributions around the highest peak from the sub-peaks, in order to mis-select sub-peaks which have peak-heights contaminated by the smoothed distribution of the main halo. We here assume that the extended galaxy distribution is the same as the average distribution appeared in the stacked galaxy maps. Third, if there is the third highest peak, we also subtract contamination of higher peaks. The peak findings are limited to within $r = 1.2r_{200m}$ from the CAMIRA center. With this procedure we identified 1561 single-peak clusters, 175 two-peaks clusters and 14 three-peaks clusters. The total number of the clusters is slightly smaller than the total number of CAMIRA clusters, because imaging data for our subhalo search are missing in some clusters. Since we cannot resolve internal structures within the FWHM, there may be closed-pair clusters whose separations are smaller than the FWHM in the single-peak cluster catalog, although they are not the majority considering its low chance probability. Furthermore, since all real clusters have internal structures, the single-peak clusters potentially contain less massive subhalos whose peak heights are under the detection limit. We therefore refer to them as “single” clusters rather than “relaxed” clusters. We also refer to two- and three-peaks clusters as “merging” clusters for simplicity. This method has a problem of the projection effect that the distributions of the main and sub clusters along the line-of-sight is highly degenerate. Therefore, the galaxy distribution alone cannot distinguish whether the main clusters and the subhalos are really interacting or not. The purity of the subhalos is discussed in Secs 3.2 and 3.3.

Given the subsamples, we carry out galaxy, weak-lensing, SZE, X-ray, and radio analyses to statistically understand their physical properties. Throughout the paper, all the observables

will be discussed using the overdensity radius $r_{200} \sim 0.7r_{200m}$, where r_{200} is the radius at which the mean enclosed density is 200 times the critical mass density of the universe at a cluster redshift. Fig. 1 shows typical examples of galaxy maps of single and merging clusters at $z \sim 0.3$.

2.2 Weak-lensing Analysis

We measure average weak-lensing masses of the merging and single clusters using a method of Point Spread Function (PSF) correction known as re-Gaussianization (Hirata & Seljak 2003), which is implemented in the HSC pipeline (see details in Mandelbaum et al. 2018). For the weak-lensing analysis, we use only galaxies satisfying with full-color and full-depth condition from the HSC galaxy catalog to achieve both precise shape measurement and photometric redshift estimation. Therefore, the weak-lensing analysis is carried out subsets of the full sample of CAMIRA clusters. We select background galaxies behind each cluster in the four-bands magnitude (*griz*) plane, following Medezinski et al. (2018).

In order to measure an average mass distribution over a subsample, we compute stacked lensing signals. For this purpose, we measure the reduced tangential shear $\langle \Delta\Sigma_+ \rangle$ computed by azimuthally averaging the measured tangential ellipticity, e_+ , for a pair of i -th galaxy and j -th cluster (Mandelbaum et al. 2006; Johnston et al. 2007),

$$\langle \Delta\Sigma_+ \rangle(r_k) = \frac{\sum_{ij} e_{+,i} w_{i,j} \langle \Sigma_{cr}(z_{l,j}, z_{s,i}) \rangle^{-1}}{2R(1+K) \sum_{ij} w_{i,j}}, \quad (1)$$

where tangential ellipticity is

$$e_+ = -(e_1 \cos 2\varphi + e_2 \sin 2\varphi). \quad (2)$$

The radius positions, r_k , are computed by the weighted harmonic mean (Okabe & Smith 2016) of radial distances from peak positions of the number density maps. The inverse of the mean critical surface mass density for individual pairs between i -th galaxy and j -th cluster is computed by the probability function $P(z)$ from the machine learning method (MLZ; Carrasco Kind & Brunner 2014) calibrated with spectroscopic data (Tanaka et al. 2018),

$$\langle \Sigma_{cr}(z_{l,j}, z_{s,i}) \rangle^{-1} = \frac{\int_{z_{l,j}}^{\infty} \Sigma_{cr}^{-1}(z_{l,j}, z_{s,i}) P(z_{s,i}) dz_{s,i}}{\int_0^{\infty} P(z_{s,i}) dz_{s,i}}. \quad (3)$$

Here, $z_{l,j}$ and $z_{s,i}$ are the cluster and source redshift, respectively. The critical surface mass density is $\Sigma_{cr} = c^2 D_s / 4\pi G D_l D_{ls}$, where D_s and D_{ls} are the angular diameter distances from the observer to the sources and from the lens to the sources, respectively. The weighting function is given by

$$w_{i,j} = \frac{1}{e_{rms,i}^2 + \sigma_{e,i}^2} \langle \Sigma_{cr}(z_{l,j}, z_{s,i}) \rangle^{-1}. \quad (4)$$

where e_{rms} and σ_e are the root mean square of intrinsic ellipticity and the measurement error per component ($\alpha = 1$ or 2),

respectively. The shear responsivity, R , and the calibration factor, K , are computed by $R = 1 - \sum_{ij} w_{i,j} e_{rms,i}^2 / \sum_{ij} w_{i,j}$ and $K = \sum_{ij} m_i w_{i,j} / \sum_{ij} w_{i,j}$, respectively. Here m_i is the multiplicative shear calibration factor for individual objects (Mandelbaum et al. 2017, 2018; Miyatake et al. 2018). We also conservatively subtract an additional, negligible offset term for calibration factor (Miyaoka et al. 2018).

In order to investigate the dynamical dependence of the average halo concentration, we use an NFW profile (Navarro et al. 1996) for model fitting. The NFW profile is expressed in the form:

$$\rho_{NFW}(r) = \frac{\rho_s}{(r/r_s)(1+r/r_s)^2}, \quad (5)$$

where ρ_s is the central density parameter and r_s is the scale radius. We measure weak-lensing masses M_{200} rather than M_{200m} . The spherical mass and the halo concentration are defined by $M_{200} = 4\pi 200 \rho_{cr} r_{200}^3 / 3$ and $c_{200} = r_{200} / r_s$, respectively.

The reduced shear model, f_{model} , is expressed in terms of the differential surface mass density $\Delta\tilde{\Sigma}$ and the local surface mass density Σ as follows,

$$f_{model} = \Delta\tilde{\Sigma}(1 + \mathcal{L}_z \Sigma), \quad (6)$$

where $\mathcal{L}_z = \sum_{ij} \langle \Sigma_{cr,ij}^{-1} \rangle w_{i,j} / \sum_{ij} w_{i,j}$. To keep the linearity for the ensemble average, we use $(1 + \mathcal{L}_z \Sigma)$ as the non-linear correction term instead of $(1 - \mathcal{L}_z \Sigma)^{-1}$. Given the mass model, the log-likelihood is described by

$$-2 \ln \mathcal{L} = \ln(\det(C_{nm})) + \sum_{n,m} (\Delta\Sigma_{+,n} - f_{model}(r_n)) C_{nm}^{-1} (\Delta\Sigma_{+,m} - f_{model}(r_m)), \quad (7)$$

where the covariance matrix, C , is composed of the uncorrelated large-scale structure (LSS) C_{LSS} , along the line-of-sight (Schneider et al. 1998) and the shape noise C_g . In model fitting, we adopt the Markov chain Monte Carlo (MCMC) method with flat priors of $\log 10^{-5} < \log(M_{200}/10^{14} h_{70}^{-1} M_{\odot}) < \log 50$ and $\log 10^{-5} < \log(c_{200}) < \log 30$. Although all quantities are the average values over the subsamples, we express them without the bracket, $\langle \rangle$, in this paper.

We also implement the lensing signal from the merging subhalos in the modeling in order to estimate their average masses, $M_{200}^{(sh)}$. We fix the positions of the subhalos and compute the lensing signal from the cluster center using an off-centering effect (Yang et al. 2006). In computations of the lensing model from the subhalos, there are two important considerations. First, all the optically-identified clusters do not always fulfill the full-color and full-depth condition for weak-lensing analysis in the HSC-SSP survey. Second, the number of background galaxies and its lensing efficiency are different for different clusters. In order to consider the lensing contributions in the stacked lensing signal, we introduce a weighting function of each subhalos associated with the j -th cluster, specified by

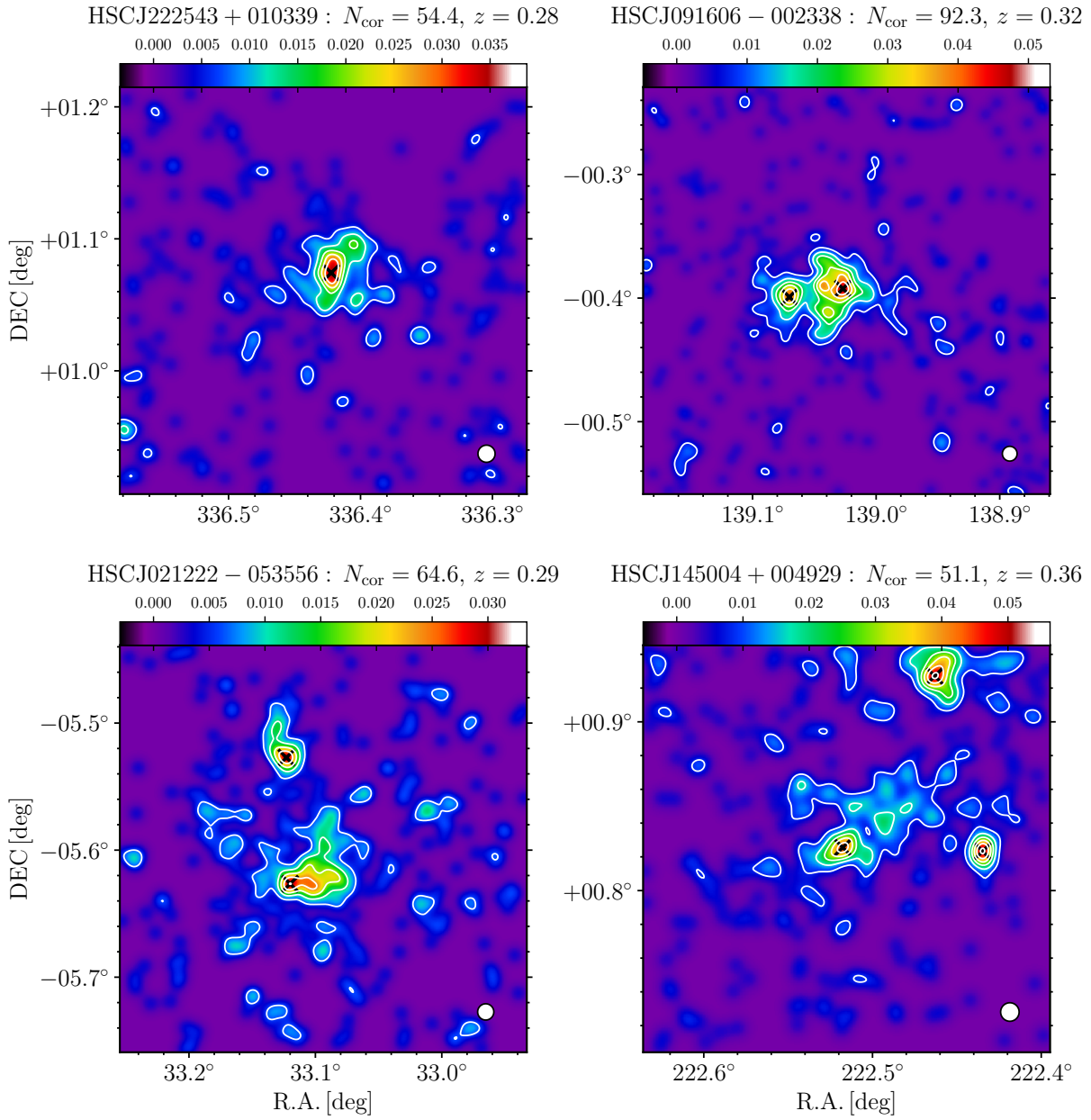


Fig. 1. Examples of galaxy maps centered the CAMIRA positions. Smoothing scale, $\text{FWHM} = 200h_{70}^{-1}$ kpc, are shown as white circles in the lower-right corners. Overlaid are contours corresponding to the number of galaxies, starting from 2 galaxies per pixel and stepping by a galaxy per pixel at each redshift. Black crosses denote galaxy peak positions. The color bar denotes the number of galaxies per a pixel. *Top-left*; the single cluster, HSCJ222543+010339. *Top-right*; the merging cluster, HSCJ091606-002338, as an example of peak-separations of $0.2h_{70}^{-1}$ kpc $< d_{\text{sh}} < 0.6h_{70}^{-1}$ kpc. Here, d_{sh} is the projected distance of galaxy subhalo from the highest peak. *Bottom-left*; the merging cluster, HSCJ021222-053556, as an example of peak-separations of $0.6h_{70}^{-1}$ kpc $< d_{\text{sh}} < 1.2h_{70}^{-1}$ kpc. *Bottom-right*; the merging-cluster, HSCJ145004+004929, as an example of peak-separations of $1.2h_{70}^{-1}$ kpc $< d_{\text{sh}} < 2.4h_{70}^{-1}$ kpc.

$$W_j = \frac{\sum_i w_{i,j}}{\sum_{i,j} w_{i,j}}, \quad (8)$$

where $w_{i,j}$ is defined by equation (4). We mention that the weighting function is also considered in estimation of other observables (eqs. 11 and 12; Secs 2.4, 2.5 and 3.5) for a comparison of weak-lensing masses. Given radial distances of the subhalo, $r_{\text{sh},j}$, in the j -th cluster, the surface mass density for the subhalos is computed by

$$\Sigma_{\text{NFW}}^{(\text{sh})}(r) = \frac{1}{2\pi \sum_j W_j} \sum_j \int_0^{2\pi} d\theta W_j \Sigma(\sqrt{r^2 + r_{\text{sh},j}^2 - 2rr_{\text{sh},j} \cos \theta}). \quad (9)$$

By integrating the above equation from 0 to r , we calculate the averaged mass density, $\bar{\Sigma}_{\text{NFW}}^{(\text{sh})}(< r)$, and subsequently obtain the reduced shear $f_{\text{NFW}}^{(\text{sh})}$. It is very difficult to constrain the concentration parameter for the merging subhalos because of a degeneracy with the lensing signal from the main cluster. We therefore fix c_{200} for the subhalos based on the best-fit concentration parameter for the single clusters and adopt a single parameter $M_{200}^{(\text{sh})}$ for the subhalos. The model for the total mass components can be expressed by

$$f_{\text{model}} = f_{\text{NFW}} + f_{\text{NFW}}^{(\text{sh})}. \quad (10)$$

We carry out weak-lensing analysis in physical unit rather than comoving unit in order to avoid a $(1+z)$ stretch of subhalo distributions found in physical unit and contamination of unknown structures in lensing profiles as much as possible. Since all other observables that are compared with lensing masses correctly take account of the lensing weight (eq. 8), the unit in weak-lensing measurements does not matter in this paper.

2.3 Red fraction

We estimate the fraction of red cluster member galaxies to all cluster member galaxies (the red fraction) of each cluster using MLZ photometric redshifts of galaxies (Tanaka et al. 2018). We define member galaxies within 1Mpc of each cluster center so that 95% confidence interval of the photometric redshifts falls in the cluster photometric redshift obtained by the CAMIRA catalog. In our analysis, we use only member galaxies whose z -band magnitudes are brighter than that of red sequence galaxies with stellar mass $M_* = 10^{10.45} M_\odot$, computed by the CAMIRA algorithm. This magnitude cut enables us to consistently determine the red fraction over all redshift range $0.1 < z < 1.1$. We divide member galaxies into red and blue cluster members based on the HSC photometry using the criteria shown in Fig. 2 of Oguri et al. (2018). In order to subtract the foreground and background contamination, for each cluster we estimate the average number densities of red and blue galaxies at the cluster redshift from the numbers of red and blue galaxies in the annulus of $1-3h_{70}^{-1}$ Mpc around the cluster center, and use them

to subtract the foreground and background contamination for estimating the red fraction (i.e., the number ratio of red to total member galaxies after the subtraction) of each cluster. We stress that the peak-finding method and its galaxy selection in our definition of the merging clusters are different from the estimation of the red fractions, and thus reasonably assume that there is no correlation between the red fractions and the subsample definitions. The result is shown in Sec. 3.4.

2.4 Stacked *Planck* SZE analysis

We use the NILC (Needlet Internal Linear Combination; Remazeilles et al. 2013) and MILCA (Modified Internal Linear Combination Algorithm; Hurier et al. 2013) all-sky Compton parameter maps (y -map, hereafter) released by Planck Collaboration et al. (2016). This y -map was constructed from the multiple Planck frequency channel maps, by characterizing in terms of noise properties and residual foreground contamination. We apply 60% Galactic and point-source masks provided by the Planck Collaboration to reduce contamination from galactic emission and point sources. Both the y -map and mask are provided in the HEALPix format (Górski et al. 2005).

We compute a noise-weighted y -map (Planck Collaboration et al. 2011) around the highest peaks in physical scale unit. In the stacking procedure, we additionally use a weight function of lensing contributions (eq 8) in order to make a fair comparison between SZE observables and weak-lensing masses, M_{200} . This is because the full-color and full-depth condition is not always satisfied with all the subsamples of the CAMIRA clusters (see Oguri et al. 2018, for details) and the lensing contributions of individual clusters in the average mass measurements are different (Sec 2.2). Given the y -map (y) and the standard deviation map (σ_y), we project each y -map of the subsample onto a two dimensional rectangular grid using a nearest neighbour interpolation,

$$\langle y \rangle_i = \frac{\sum_j y_{i,j} \sigma_y^{-2} W_j}{\sum_j \sigma_y^{-2} W_j}, \quad (11)$$

where the subscript, j , denotes the cluster. Since a y -map resolution is poor with the circular Gaussian beam of FWHM= 10 arcmin, Y_{SZ} are measured within a cylindrical circle $2r_{200}$ centered at peak positions weighted with the stacked $\langle y \rangle$. The measurement errors of Y_{SZ} include the statistical noise, bootstrap sampling errors and aperture sizes caused by weak-lensing measurement uncertainty. We represent the result and discussion in the Sec 3.6.

2.5 Stacked RASS analysis

We stack the X-ray emission from the position-sensitive proportional counter (PSPC) of ROSAT all-sky survey (RASS) in the 0.12.4 keV band (Truemper 1982), in a similar manner to

the stacked *Planck* SZ images (Sec. 2.4). We exclude regions of point sources, from the second ROSAT all-sky survey source catalogue (the 2RXS catalogue; Boller et al. 2016), which are not statically associated with galaxy density peaks. The excluded radius is four times the 1σ size of the PSF. A point spread function is empirically estimated by stacking the RASS images of 2RXS point sources located within one degree centering main peaks of individual clusters. We stack count images as well as the corresponding RASS exposure map (Anderson et al. 2015) and then compute count rate images. Since our targets are located at low Galactic column density region, the galactic absorption at each cluster field is not significantly changed. As a weighing function, we use $D_L^2(z_i)/D_L^2(z_{\text{ref}})$ and the lensing contribution W (eq. 8) in order to standardize the flux to its expectation at the average redshifts of weak-lensing samples, for the purpose of the L_X and M_{200} scaling relation study (Miyazaki et al. 2018a). Here, D_L is the luminosity distance to the clusters and z_{ref} is the reference redshift. To avoid a positional fluctuation of the background component caused by unknown sources, we estimate the background component by fitting the radial profiles. We measure the aperture photometry for the stacked images within r_{200} and subtract the background components. Assuming the metallicity $Z = 0.2$ and $k_B T = 1.9$ keV (Vikhlinin et al. 2009), we convert the estimated count rate to the X-ray luminosity, L_X . The measurement uncertainty is composed of the statistical noise assuming Poisson errors, bootstrap sampling errors, and aperture sizes caused by weak-lensing mass uncertainty. We represent the result and discussion in the Sec 3.6, including the *Planck* SZE and mass scaling relation.

3 Result and Discussion

3.1 Halo concentration and mass ratio

We study a difference of halo concentrations between the single and merging clusters based on weak-lensing analysis (Sec 2.2). Left panel of Fig. 2 shows posterior distributions of the two subsamples by weak-lensing analysis. Assuming a single NFW component for both the single and merging clusters, the best-fit concentration parameters for the single and merging clusters are $c_{200}^{\text{single}} = 2.92_{-0.41}^{+0.48}$ and $c_{200}^{\text{merger}} = 1.98_{-0.35}^{+0.41}$, respectively. The average redshift of the two samples are similar ($z^{\text{single}} = 0.38$ and $z^{\text{merger}} = 0.37$). The best-fit mass for the single clusters, $M_{200}^{\text{single}} = 1.48_{-0.25}^{+0.29} \times 10^{14} h_{70}^{-1} M_{\odot}$, is about half of the merging clusters, $M_{200}^{\text{merger}} = 2.98_{-0.48}^{+0.55} \times 10^{14} h_{70}^{-1} M_{\odot}$. Although the concentration parameter depends weakly on the halo mass (e.g. Bullock et al. 2001; Duffy et al. 2008; Ludlow et al. 2012; Bhattacharya et al. 2013; Meneghetti et al. 2014; Ludlow et al. 2014; Diemer & Kravtsov 2015; Child et al. 2018), the difference of the two masses is negligible in the following discussion of the halo concentration.

A recent numerical simulation (Child et al. 2018) defined relaxed clusters and unrelaxed clusters using a distance between the halo center and the center of mass of all particles. In the left panel of Fig. 2, the solid blue line and filled blue area denote the average concentration for the simulated, relaxed clusters and its 1σ scatter computed at M_{200}^{single} and z^{single} , respectively. Our best-fit concentration for the single clusters is somewhat lower than a prediction of the numerical simulation, though they are consistent within intrinsic scatter. Child et al. (2018) have also shown that the concentration of the unrelaxed clusters is 69 per cent lower than that of the relaxed clusters at $z = 0$ (Figure 3 in their paper). The dotted red line and filled blue area are the average concentration for the unrelaxed clusters and its 1σ scatter, assuming $c_{200}^{\text{unrelaxed}}/c_{200}^{\text{relaxed}} = 0.69$ at $z = 0$. Our result gives $c_{200}^{\text{merger}}/c_{200}^{\text{single}} = 0.68 \pm 0.17$, in agreement with Child et al. (2018). Neto et al. (2007) show that the concentration of the unrelaxed clusters is ~ 66 per cent of the relaxed clusters at our best-fit mass range. Similarly, other numerical simulations (e.g. Duffy et al. 2008; Bhattacharya et al. 2013) have pointed out that the halo concentration of the full sample of simulated clusters is lower than that of the relaxed clusters.

We study whether the halo concentration depends on the peak separation or not. Since the overdensity radius of the merging clusters is $r_{200} = 1.22 \pm 0.07 h_{70}^{-1}$ Mpc, we divide the merging cluster sample into three subsamples with the projected distances of subhalos, d_{sh} , in $[0.2, 0.6]$, $[0.6, 1.2]$, and $[1.2 - 2.4] h_{70}^{-1}$ Mpc. The number of the subsamples and the actual number of the WL clusters are summarized in Table 1. Five clusters out of the 189 merging clusters fall from the radial ranges. We adopt the closest distance for the three-peaks clusters in the subsample selection. The right panel of Fig. 2 shows the concentration parameter as a function of projected distances of subhalos, d_{sh} . When the projected distance of subhalos are less than r_{200} , the concentration parameters are underestimated by $\sim 50 - 70$ per cent compared to the single clusters. Furthermore, the best-fit concentration parameter decreases as the subhalo distance increases. When the subhalos are located outside r_{200} , the concentration parameter is comparable to that of the single clusters. This trend can be naturally explained by the position of the subhalos, because merging clusters, which have subhalos at larger radii, tend to possess a less centrally concentrated profile. On the other hand, mass components outside clusters do not affect the internal structure of the targeting clusters.

Next we model the two NFW components as the main and subhalos for the merging clusters (eqs 9 and 10). Since the concentration parameter of the subhalos is not well determined, we assume $c_{200} = 3$ from the best-fit of the single clusters. When we change $c_{200}^{(\text{sh})}$ by ± 1 , the subhalo masses are changed by only by $\lesssim 10\%$. Fig. 3 shows stacked lensing profiles of the three subsamples of the merging clusters. The total mass component

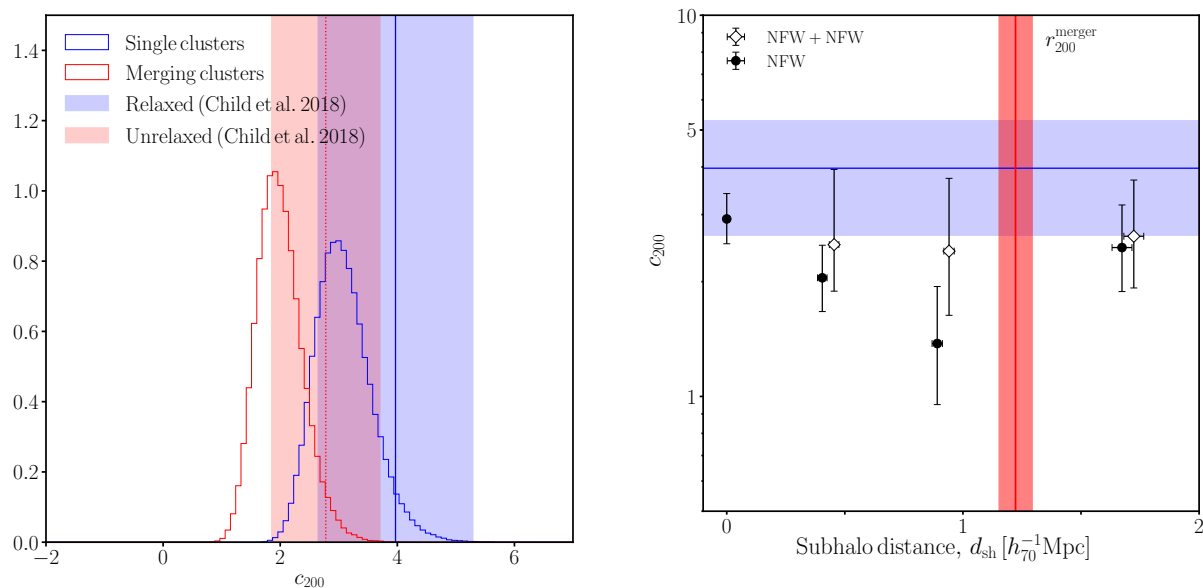


Fig. 2. *Left:* Posterior distributions of halo concentrations for single (blue) and merging (red) clusters. The solid blue line and filled blue area are a prediction and 1σ scatter of relaxed clusters at $z = 0.38$ (Child et al. 2018), respectively. The dotted red line denotes a prediction of an unrelaxed sample of clusters of Child et al. (2018), $c_{200}^{\text{unrelaxed}}/c_{200}^{\text{relaxed}} = 0.69$, expected from their result at $z = 0$. The filled red area is 1σ scatter of unrelaxed clusters. *Right:* The halo concentration, c_{200} , as a function of projected distances of subhalos, d_{sh} . The vertical red line and region are the best-fit r_{200} of the total mass of all the merging clusters and its 1σ uncertainty, respectively. The horizontal blue region is the same as the left panel. Black circles denote the best-fit NFW model. When the subhalos are located inside r_{200} on the sky, the concentration parameter decreases as the subhalo distance increases. In contrast, the concentration of the merging clusters with subhalos of $d_{\text{sh}} > r_{200}$ is comparable to that of the single clusters. White diamonds are the concentration parameter of the main halo modeled with the two NFW components for the main and sub halos. The concentration parameters are recovered when the subhalo component is considered.

Table 1. Subsamples: ^a The signal-to-noise ratio of weak-lensing signal computed by $(S/N)_{\text{WL}} = (\Delta\Sigma_{+,n} C_{nm}^{-1} \Delta\Sigma_{+,m})^{1/2}$ where C is the error covariance matrix $C_g + C_s + C_{\text{LSS}}$.

merging clusters		
$d_{\text{sh}} [h_{70}^{-1} \text{Mpc}]$	$(S/N)_{\text{WL}}^a$	Number of WL/total clusters
0.2 – 0.6	13.0	46/53
0.6 – 1.2	10.9	61/68
1.2 – 2.4	8.8	57/63
single clusters		
N_{cor}	$(S/N)_{\text{WL}}^a$	Number of WL/total clusters
15 – 18	11.3	464/552
18 – 21	11.6	272/316
21 – 25	12.6	245/283
25 – 30	12.9	164/191
30 – 40	12.9	137/156
40 – 100	16.7	53/63

is shown by red thick lines. The main and subhalo components are shown by dashed blue and dotted green lines, respectively. Clear bumps in the stacked lensing profiles are found associated with the positions of the subhalos. It indicates that the mass is indeed associated with the galaxy subhalos detected by the peaks in the galaxy maps (Fig. 1). The bump is caused by the off-centering effect (Yang et al. 2006). The concentration parameters for the main halo components are shown by white diamonds in the right panel of Fig. 2. In contrast to one NFW component analysis, the estimated concentration parameter is almost constant against the subhalo distances. The values are in good agreement with that of the single clusters. Thus, once the subhalo component is considered in the modeling, the halo concentration is recovered.

We also estimate the mass ratios for the three subsamples; $M_{\text{sh}}/M_{\text{main}} = 0.37^{+1.02}_{-0.26}$, $0.47^{+0.91}_{-0.28}$ and $0.14^{+0.27}_{-0.11}$ from small to large separations, respectively. The measurement uncertainty of the mass ratio takes into account the covariance error matrix between two mass components. Since the mass estimations of the main and subhalos are highly correlated, the errors of the mass ratio are relatively large. Similarly, we repeat the two-halo modeling for the all merging clusters at $0.2 h_{70}^{-1} \text{Mpc} < d_{\text{sh}} < 2.4 h_{70}^{-1} \text{Mpc}$ and obtain $M_{\text{sh}}/M_{\text{main}} = 0.31^{+0.68}_{-0.20}$. The average value of the mass ratios for the three subsamples is 0.33,

where the lensing weight (eq. 8) is considered. Since we fix the positions of the subhalos and the halo concentration, the subhalo mass is sensitive to the lensing amplitude and thereby the mass ratios with and without subdivisions are consistent with each other. The mass ratio is smaller than the ratio, 0.75 ± 0.18 , of peak heights appeared in the galaxy maps. Considering measurement uncertainty, the majority of our sample of the merging clusters is major mergers with the mass ratio at order of $\gtrsim 0.1$.

We note that the projection effect of surrounding halos is not large at $r \lesssim r_{200}$ as we will discuss in Secs 3.2 and 3.3. Thus, the weak-lensing mass and halo concentration for the merging clusters at $d_{\text{sh}} < r_{200}$ can be interpreted as results affected by the internal subhalos.

We ignored mis-centering effect (e.g. Yang et al. 2006; Johnston et al. 2007; Okabe et al. 2013) on the halo concentration in the above discussion. The density peaks do not necessarily correspond to the center of halo mass. If there were offsets between density peaks and mass centers, concentration parameters would be underestimated by mis-centering effect. However, since the concentration parameters of the main halos of the merging clusters (two NFW modeling) agree with that of the single clusters (the right panel of Fig. 2), both the merging and single clusters would have similar distribution of offset distances if they exist. Although the mis-centering effect might affect the absolute value of concentration parameters, it does not significantly affect the comparison of how much halo concentrations are relatively affected by the subhalos. Modeling with the mis-centering effect would be important to precisely measure the mass-concentration relation, which is left for future works.

3.2 Projected number density

The projected average number density of cluster subhalos as a function of projected distances from the main peaks is shown in the left panel of Fig. 4. As expected, the optically-identified, massive subhalos are widely distributed from cluster centers to outskirts. The errors for the projected number density are assumed to be Poisson noise. The projected number density is well described by a β model, formed by $\Sigma_{\text{sh}}^n \propto (1 + (r/r_c)^2)^{0.5-\beta}$. The corresponding three-dimensional number density is written as $n \propto (1 + (r/r_c)^2)^{-\beta}$. The best-fit parameters (the blue curve) are $r_c = 0.45^{+0.52}_{-0.22} h_{70}^{-1}$ Mpc and $\beta = 1.20^{+0.45}_{-0.16}$, giving an outer slope of $n \propto r^{-2.4}$.

We note that our selection of the subhalos may suffer from the projection effect. Hence, the projection of galaxy concentrations along the line-of-sight appears in the radial profile. As a simple test, we introduce an additional constant parameter, $\Sigma_{\text{proj}}^{(n)}$ as the projection-effect component. The best-fit parameters are $r_c = 0.85^{+0.62}_{-0.44} h_{70}^{-1}$ Mpc, $\beta = 2.18^{+2.56}_{-0.76}$ and $\Sigma_{\text{proj}}^{(n)} = 0.045^{+0.023}_{-0.027} h_{70}^2 \text{Mpc}^{-2} \text{cluster}^{-1}$. The best-fit radial

distribution of subhalos excluding the projection effect is shown in the dashed-dotted magenta line. The project effect is small at $r \lesssim r_{200}$, whereas it accounts for about a half of detected subhalos at $r \gtrsim r_{200}$.

The projected mass density profile of the main halo of the merging clusters is shown by red line. We use the best-fit NFW model for the full sample of the merging clusters modeled with two-halo components. The profile is normalized by $\int_0^{r_{200}} dr 2\pi r \Sigma_{\text{NFW}} = 1$. Here, r_{200} for the main cluster is derived from the two-halo component fit described in Secs. 2.2 and 3.1. The radial profile of the subhalos is significantly shallower than the total matter distribution, as predicted by theoretical works (e.g. Gao et al. 2004; Diemand et al. 2004; Nagai & Kravtsov 2005; Taylor & Babul 2005; Ludlow et al. 2009; Han et al. 2016). The radial distribution of subhalos within their parent halos is less centrally concentrated than that of dark matter. Subhalos captured by more massive halos are subject to dynamical friction, losing their angular momentum and subsequently falling inward the center. Simultaneously, their masses are reduced by the tidal force which increases with an increasing radius from the cluster center. Diemand et al. (2004) and Gao et al. (2004) find that the radial distribution of subhalos is largely independent of their self-bound mass, which is caused by an efficient mixing of the above physical process of the evolution of subhalos within the potential of the main halo. Han et al. (2016) propose an analytic model which simultaneously predicts both the mass function and spatial distribution of subhalos, considering statistical description of the amount of mass tidally stripped from individual subhalos. They find that the model radial profile agrees with results of numerical simulations. We compute a surface number density of subhalos using SUBGEN (Han et al. 2016) with their final mass higher than 10 per cent of the main halo with $M_{200} = 10^{14} h^{-1} M_{\odot}$ and $c_{200} = 3$. The model profile normalized by the total number of subhalos is shown by green dashed line. The observed profile at $r < r_{200}$ is in an agreement with the prediction, but is somewhat shallower outside r_{200} . On the other hand, the dashed-dotted magenta profile, for which the projection effect is corrected, is in a good agreement with the theoretical prediction over a wide radial range.

Numerical simulations (e.g. Neto et al. 2007; Ludlow et al. 2012) defined relaxed and unrelaxed clusters using the following three criteria; subhalo mass fraction, center of mass displacement, and ratio of kinetic energy to gravitational energy. They found that the fraction of unrelaxed halos are roughly ~ 30 percent and increases as the halos masses increase. The fraction of unrelaxed clusters also depends on resolutions of numerical simulations. Our sample of the merging clusters account for ~ 10 percent of the total sample. Since the two definitions are different, a fair comparison is difficult but our fraction is lower than expected by numerical simulations. We inves-

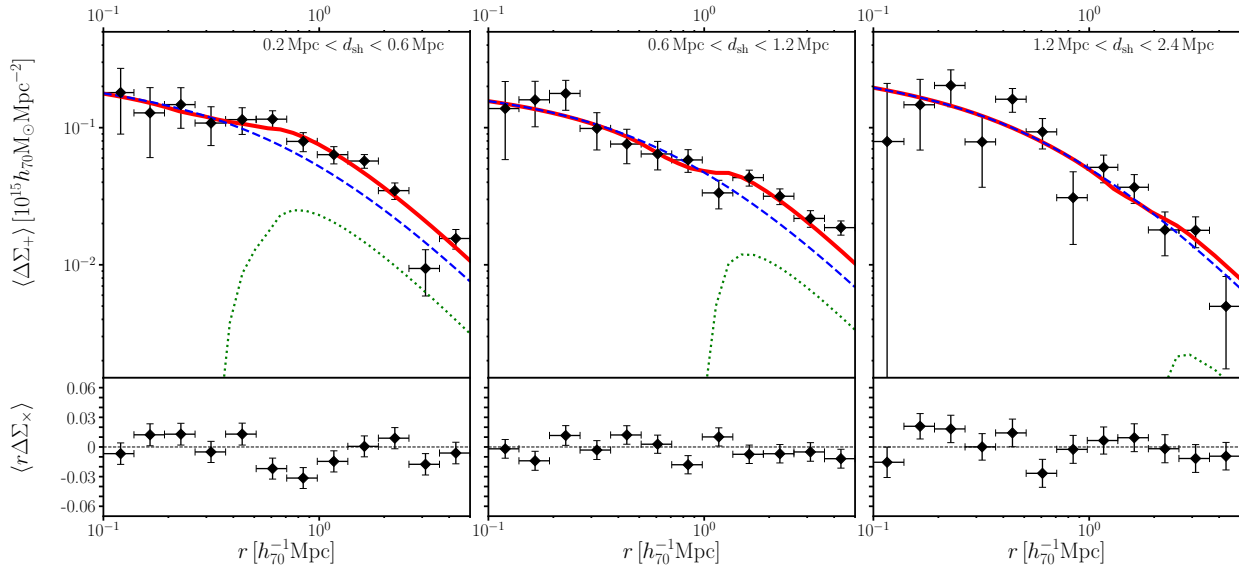


Fig. 3. *Top:* The stacked tangential shear profile for the three subsamples of the merging clusters. The subsamples are defined by the subhalo distances of $0.2h_{70}^{-1} \text{Mpc} < d_{\text{sh}} < 0.6h_{70}^{-1} \text{Mpc}$, $0.6h_{70}^{-1} \text{Mpc} < d_{\text{sh}} < 1.2h_{70}^{-1} \text{Mpc}$, and $1.2h_{70}^{-1} \text{Mpc} < d_{\text{sh}} < 2.4h_{70}^{-1} \text{Mpc}$, respectively. The errors are composed of the diagonal component of $(C_g + C_s + C_{\text{LSS}})^{1/2}$. Solid red, dashed blue, and dotted green lines are the total mass model, the NFW model for the main halo and the subhalo mass, respectively. *Bottom:* The product of the 45 degree rotated component, $\Delta\Sigma_{\times}$, as a function of the cluster-centric radius, r .

tigate mass dependence of the merger fraction and find ~ 50 percent for $M_{200} > 5 \times 10^{14} h_{70}^{-1} M_{\odot}$, ~ 25 percent for $M_{200} \sim 3 \times 10^{14} h_{70}^{-1} M_{\odot}$, and ~ 10 percent for $M_{200} \sim 10^{14} h_{70}^{-1} M_{\odot}$. This trend would be explained by the peak-finding technique. Less massive clusters have smaller number of galaxies, and thus sparse distributions of a small number of galaxies give rise to the possibility that peak-heights of some subhalos are below the threshold. Therefore, some subhalos of the order of $\sim 10^{13} h_{70}^{-1} M_{\odot}$ in halos of $\sim 10^{14} h_{70}^{-1} M_{\odot}$ halos might be not identified by the current technique. Using a larger number of clusters in the future HSC-SSP dataset, we will develop more sophisticated detection schemes and discuss the purity of the merger sample especially for less massive clusters.

3.3 Velocity-space diagram

We compute a velocity-space diagram of the subhalos stacked over the merging clusters (right panel of Fig. 4). The spectroscopic data is retrieved from the SDSS DR14 (Abolfathi et al. 2018). We compute the average line-of-sight velocity around the each galaxy peak within $200h_{70}^{-1} \text{kpc}$ and regard it as the velocity of the main and sub halos. The deviations of the line-of-sight velocities of the subhalos from the main halo are shown by large red circles. As a reference, spectroscopic galaxies around the single and merging clusters are overlaid. Many galaxies are confined within the characteristic, “trumpet”, shape expected in the spherical infall model (e.g. Kaiser 1987; Diaferio & Geller

1997; Mamon et al. 2013). The caustic amplitude computed by the weak-lensing mass of the main halo for the merging clusters is shown in the solid red line. Most subhalos (30 subhalos) are located within the caustics surfaces, indicating that they are indeed physically interacted with the main halo. On the other hand, a few subhalos are located outside the caustic surface, and thus contaminating components caused by the projection effect. The fraction of the contamination is consistent with that estimated from the subhalo radial profile (the left panel of Fig. 4).

3.4 Red fraction

We statistically investigate, using the optically-selected cluster sample, whether the red fraction is changed by cluster mergers or not. As mentioned in Sec 2.3, we use the massive galaxies, with $M_{*} > 10^{10.45} M_{\odot}$, which are centrally concentrated inside the clusters. We subtract the numbers of red and blue galaxies in the annulus $(1 - 3h_{70}^{-1} \text{Mpc})$ to compute the red fraction (Sec. 2.3). The inner radius is comparable to $r_{200}^{\text{single}} = 0.95 \pm 0.06 h_{70}^{-1} \text{Mpc}$ for the single clusters and $r_{200}^{\text{merger}} = 1.22 \pm 0.07 h_{70}^{-1} \text{Mpc}$ for the merging clusters ($r_{200}^{\text{merger,main}} = 1.07 \pm 0.10 h_{70}^{-1} \text{Mpc}$ for the main halo), determined by the weak-lensing analysis (Sec. 3.1). We do not find significant structures of massive galaxies outside r_{200} of the clusters except for merging clusters with large peak separations. We thus exclude the merging clusters from the three subsamples with peak separation of $d_{\text{sh}} > 1.2h_{70}^{-1} \text{Mpc}$. (Sec.

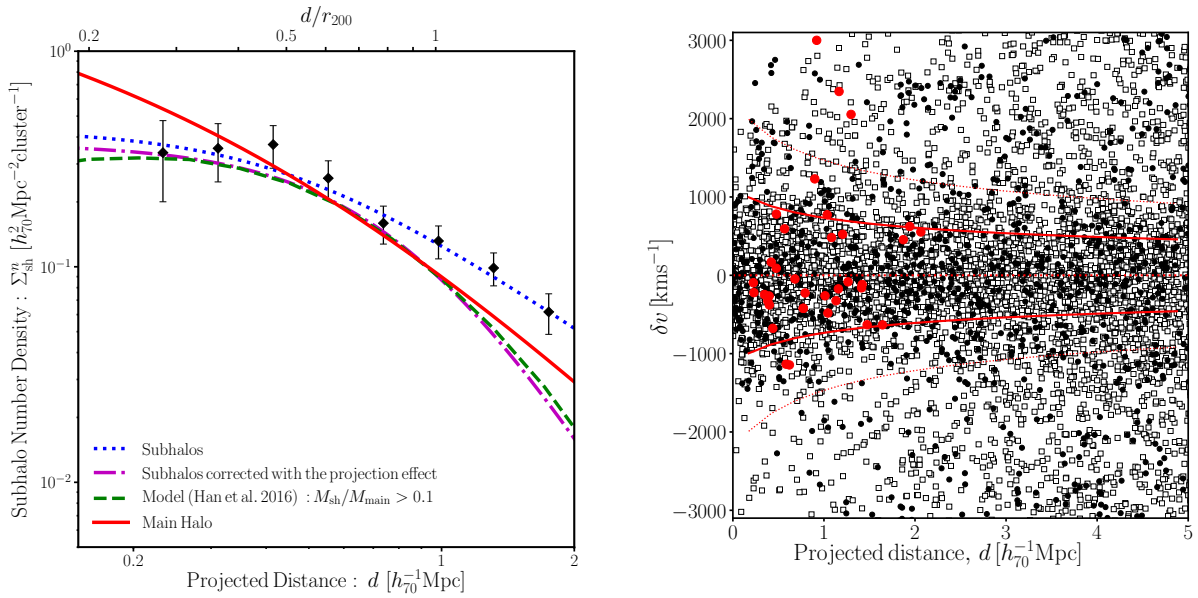


Fig. 4. *Left:* The radial profile of the averaged projected number density of the sub halos per a cluster. The dotted blue and solid red lines show the best-fit β profile of the subhalo radial profile and the NFW profile for the main cluster normalized by $\int_0^{r_{200}} dr 2\pi r \Sigma_{\text{NFW}} = 1$, respectively. The dashed-dotted magenta line is the best-fit profile for the subhalos, corrected with the projection effect. The dashed green line is the normalized project distribution for subhalos with $M_{\text{sh}}/M_{\text{main}} > 0.1$ (Han et al. 2016). *Right:* The stacked velocity-space diagram from the SDSS. White squares and black circles are spectroscopic galaxies around the single and merging clusters, respectively. Large red circles denote subhalos with spectroscopic counterparts. The thick, red solid lines are the caustic amplitude estimated by the weak-lensing mass for the main halo of the merging clusters. The thin, dotted red line denotes twice the caustic amplitude.

3.1) in order to avoid over-subtraction in the following results.

The left panel of Fig. 5 shows the redshift evolution of the average red fraction which is the ratio of red member galaxies to all member galaxies selected by their photometric redshifts. We adopt the biweight estimation in order to down-weight outliers in a small number of subsample. The uncertainties are the errors of the biweight mean. The red fractions for all the clusters gradually decreases as cluster redshifts increase, as discovered by Butcher & Oemler (1984).

We next compare, in a model-independent way, red fractions for the merging and single clusters (the left panel of Fig. 5). Since the red fraction weakly depends on cluster richness and the richness population of the merging clusters is different from that of the single clusters, we define subsamples in a redshift and richness space. The red fractions for the merging clusters are comparable to those for the single clusters, and some cases show lower values. The deviation is not statistically significant at $\lesssim 2\sigma$ level. Nevertheless, in any subsamples, the red fraction of the merging clusters does not exceed the value of the single clusters. It implies that star formation would be triggered by cluster mergers.

As a complementary approach, we fit red fractions of the merging and single clusters as a function of cluster richness and redshift and intrinsic scatter of red fractions. A functional form is simply assumed to be $f_{\text{red}} = f_{\text{red},0} + a_z z^{b_z} + a_N N_{\text{cor}}^{b_N}$. The powers of redshift and richness, b_z and b_N , are determined by

fitting all the sample. We then obtain the normalizations and slopes of the single and merging clusters by fixing the powers. The red-fraction ratio between the merging and single clusters is computed by taking account of the correlation between the errors on each parameter by calculating the error covariance matrix. The right panel of Fig. 5 shows the red-fraction ratio as a function of cluster redshift, for a fixed cluster mass. We here convert from the richness to the cluster mass based on stacked weak-lensing analysis (Sec. 3.5). Overall, the red-fraction ratios agree with unity, although the ratio for the low mass cluster of $M_{200} = 10^{14} h_{70}^{-1} M_{\odot}$ is somewhat lower. The general feature is consistent, within errors, with the aforementioned model-independent estimations. The red-fraction ratio typically decreases as the cluster redshift increases and the mass decreases. If the star formation is triggered by cluster mergers, its time-scale can be roughly estimated by the cluster size and the collision velocity and thus is $2r_{200}/v \sim 2 \text{Gyr} (v/1000 \text{kms}^{-1})^{-1}$. As mentioned above, the observational evidence is not significant. Therefore, more precise observational constraints on red fractions and their properties require larger cluster samples.

Various processes to trigger star formation during cluster mergers are proposed; the ram-pressure enhancement (e.g. Dressler & Gunn 1983; Evrard 1991; Fujita et al. 1999), a change of the gravitational tidal field (Bekki 1999), and the encounters and interactions between galaxies (Lavery & Henry 1988). The ram-pressure scenario advocates that the high ram-

pressure of the ICM compresses the hot, tenuous inter-stellar medium (ISM) in gas-rich galaxies and trigger a one-time burst of star formation, but gas stripping weakens the star-burst phenomenon during the cluster collision (e.g. Fujita et al. 1999). Ruggiero & Lima Neto (2017) investigated through numerical simulations how much of an initial gas mass in Milky-Way like galaxies is turned into stars after a single crossing of idealized clusters of 10^{14} and $10^{15} M_{\odot}$. They found that the initial gas mass is more efficiently converted to stars in less massive clusters, because the ram-pressure stripping process is more efficient in more massive clusters, making the galaxy lose its gas faster, and consequently prevent the steady star formation over the entire orbit. The general feature predicted by the numerical simulations is similar to our results of mass dependence of the red-fraction ratio. Dressler & Gunn (1983) suggested that the star formation is triggered by gas-rich galaxies first infall into the ICM, so called the first infall model. It does not contradict with the trend that the red-fraction ratio decreases as the cluster redshift increases. Even if a dusty star formation activity (Koyama et al. 2010) is triggered by cluster mergers, it does not change the interpretation that the star formation in the merging clusters is likely to be more active.

The activities of star formation in on-going merging clusters at $z \lesssim 0.4$ is studied through spectroscopic observations or narrow band filters. For instance, Stroe et al. (2015) studied star-formation rate in two merging clusters with prominent radio relics (CIZA J2242.8+5301 and IRXS J0603.3+4213). They found that the star-formation rate density for CIZA J2242.8+5301 is on the order of 15 times the peak of the star-formation history, and the overall star-formation rate density in IRXS J0603.3+4213 is consistent with blank fields at the same redshift. In CIZA J2242.8+5301, the projected distribution of highly star-forming galaxies is localized along the merger axis. Stroe et al. (2017) carried out spectroscopic observations of 19 clusters and found that the normalization of $H\alpha$ luminosity function in merging clusters is much higher than that of relaxed clusters. Ferrari et al. (2005) showed a lack of bright post-star-forming objects in A3921. Deshev et al. (2017) found a depletion of star forming galaxies within the central ~ 1.5 Mpc region of the merging clusters A520, in contrast to relaxed clusters. Therefore, the results appear to be not converged due to the large intrinsic scatter of the abundance of star forming galaxies. Indeed, our estimation of intrinsic scatter of the red fraction is large, $\sigma_{\text{red}} = 0.18$. Since our estimations are based on photometric redshifts, further systematic follow-up studies of clusters compiling various merging stages, cluster masses, and redshifts are essential to understand star formation activities in merging clusters, in order to witness short time scale variations in star formation and understand their mass and redshift dependence.

3.5 Mass - richness relation

We study the correlation between the mass and richness. Based on the weak-lensing analysis (Sec 3.1), we define the three subsamples of the merging clusters (Table 1) using peak separations of d_{sh} in $[0.2, 0.6]$, $[0.6, 1.2]$, and $[1.2, 2.4]$ Mpc. As for the single clusters, we adopt the same definition of the subsamples as that in the *Planck* SZ and mass scaling relation (Sec 3.6) because of a requirement for the stacking analysis of the *Planck* data.

The average richness for each subsample is computed with a weight assigned to the lensing contribution of the j -th cluster (eq. 8), in the same analogy as Secs 2.4 and 2.5,

$$N_{\text{cor}} = \frac{\sum N_{\text{cor},j} W_j}{\sum W_j}. \quad (12)$$

Fig. 6 shows the mass and richness relation. We use the NFW masses for the single clusters (Secs 2.2 and 3.1). Both the total masses of the two NFW components and the single NFW masses for the merging clusters are represented in the figure. We find a tight correlation between the mass and richness regardless of the mass definitions.

We assume that the scaling relation is described by the following power-law relation,

$$M_{200} E(z) = M_N \left(\frac{N_{\text{cor}} E(z)}{N_0} \right)^{\alpha}, \quad (13)$$

where $E(z) = (\Omega_{m,0}(1+z)^3 + \Omega_{\Lambda})^{1/2}$ is the evolution factor and $N_0 = 15$. We perform linear regression using their log-space variables without correcting for selection function. The intrinsic scatter of the mass, $\sigma_{\ln M}$, is considered in the fitting (Okabe et al. 2010). We obtain $M_N = 0.72_{-0.14}^{+0.18} \times 10^{14} h_{70}^{-1} M_{\odot}$, $\alpha = 1.41_{-0.22}^{+0.23}$, and $\sigma_{\ln M} < 0.08$ for the single clusters. When we include the richness and the total mass of the merging clusters, the best-fit parameters are $M_N = 0.76_{-0.14}^{+0.18} \times 10^{14} h_{70}^{-1} M_{\odot}$, $\alpha = 1.35_{-0.20}^{+0.20}$, and $\sigma_{\ln M} < 0.07$, respectively. We find in both cases a steeper slope than $M_{200} \propto N_{\text{cor}}$, which conflicts with our first assumption to make smoothed maps (Sec 2.1). However, the discrepancy does not significantly affect the subhalo search, because our maps sufficiently covered the wide area. There is no significant deviation of the merging clusters in the mass and richness relation, as seen in the small upper limit of the intrinsic scatter. It indicates that the richness is insensitive to the merger boost, as your expectations.

For future relevant papers, we explicitly note the best-fit normalizations and slopes for M_{500} and $M_{200\text{m}}$ in the form of eq. 13; $M_N = 0.46_{-0.07}^{+0.08} \times 10^{14} h_{70}^{-1} M_{\odot}$ and $\alpha = 1.43_{-0.17}^{+0.17}$ for M_{500} and $M_N = 0.95_{-0.19}^{+0.24} \times 10^{14} h_{70}^{-1} M_{\odot}$ and $\alpha = 1.41_{-0.24}^{+0.24}$ for $M_{200\text{m}}$, respectively.

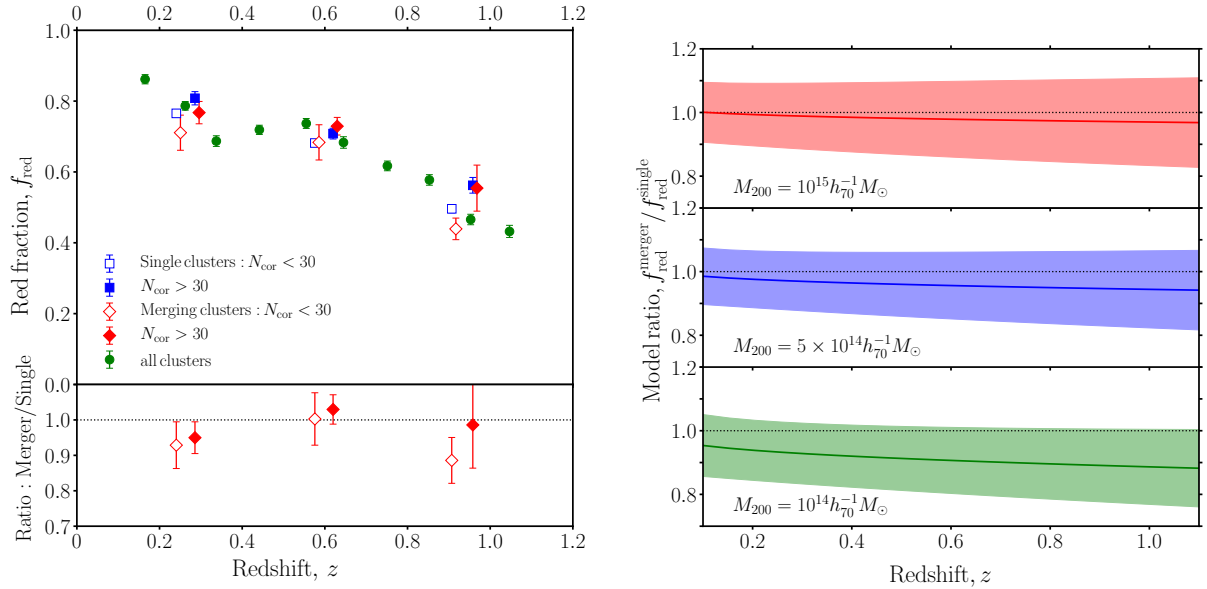


Fig. 5. *Left:* The red fraction as a function of the cluster redshift (upper panel). Green circles are the red fractions of all the clusters excluding the merging clusters of which peak separations are $d_{\text{sh}} > 1.2h_{70}^{-1}$ Mpc. Filled blue squares and red diamonds denote the red fractions of the single and merging clusters with $N_{\text{cor}} > 30$, respectively. Open blue squares and red diamonds are those with $N_{\text{cor}} < 30$. The lower panel shows ratios between red fractions of the merging and single clusters. *Right:* The model-dependent estimations of the ratio of red fractions between the merging and single clusters. The top, middle, and bottom panels are the red-fraction ratio of clusters with masses of 10^{15} , 5×10^{14} and $10^{14} h_{70}^{-1} M_{\odot}$, respectively. The solid line and color area are the best-fit and its 1σ uncertainty, respectively. The black dotted lines denote the case that the ratio is equal to unity.

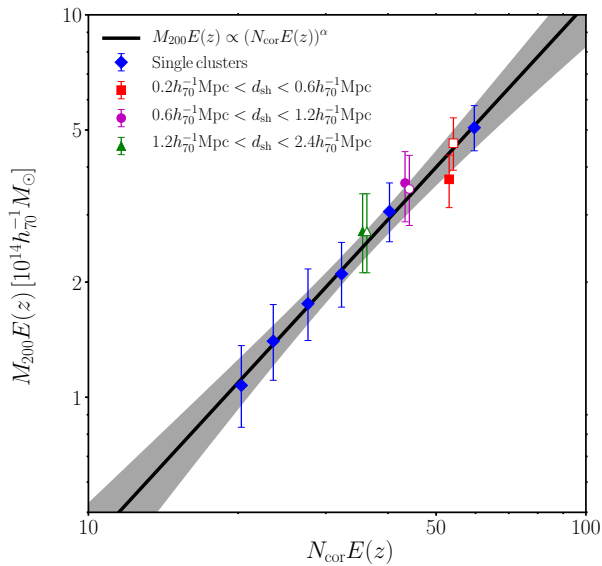


Fig. 6. Mass-richness relation. Blue diamonds denote the single clusters. Red square, magenta circle, and green triangle are the merging clusters divided by peak separations. As for the merging clusters, the solid and open symbols are the total mass and the single NFW mass, respectively. The solid and gray area denote the best-fit and its 1σ error of the scaling relation for the single clusters with a free slope.

3.6 *Planck* SZ and *ROSAT* L_X scaling relations

In this subsection, we study scaling relations between the weak-lensing masses and *Planck* SZ (Sec 2.4) and *ROSAT* X-ray luminosity (Sec 2.5) and the merger boost of the ICM.

We compute a cylindrically integrated quantity Y_{SZ} using two maps of public y map; MILCA (Hurier et al. 2013) and NILC (Remazeilles et al. 2013). We split the merging sample into three subsamples using peak separations of d_{sh} in $[0.2, 0.6]$, $[0.6, 1.2]$, and $[1.2, 2.4]$ Mpc, based on the weak-lensing analysis (Sec 3.1). As for the single clusters, we use the richness, N_{cor} , to define subsamples so that the signal-to-noise ratio of the tangential profiles for the subsamples is as uniform as possible and the number of each subsample is higher than fifty. The second condition is required to compile the sufficient number of clusters in stacked y maps. The definition of the subsample is summarized in Table 1. Since all the clusters do not always fulfill the full-depth and full-color condition for weak-lensing analysis, the stacked y measurements are computed with a weight assigned to the lensing contribution. The Y_{SZ} are measured within $2r_{200}$ determined by weak-lensing mass measurements, taking into account the large *Planck* FWHM. For the merging clusters, we use the overdensity radii of the total masses of the main and sub clusters. We obtain consistent results for the MILCA and NILC Y_{SZ} measurements (Fig. 7).

We find that the mass scaling relation with the *Planck* SZ measurements is in excellent agreement with a self-similar so-

lution (dashed line)

$$Y_{\text{SZ}}E(z) = Y_0 \left(\frac{M_{200}E(z)}{M_0} \right)^{5/3}. \quad (14)$$

We fit the scaling relation for the single clusters with a free slope parameter, $Y_{\text{SZ}} \propto (M_{200}E(z))^\alpha$, and obtain $\alpha = 1.56_{-0.23}^{+0.29}$ (NILC) and $\alpha = 1.65_{-0.23}^{+0.29}$ (MILCA), consistent with the self-similar slope. We use the lognormal quantities in the linear regression with the intrinsic scatter. The normalization is $Y_0 = 4.58_{-1.23}^{+1.41} \times 10^{-6}$ [Mpc²] at $M_0 = 10^{14} h_{70}^{-1} M_\odot$ for NILC and $Y_0 = 3.91_{-1.10}^{+1.29} \times 10^{-6}$ [Mpc²] for MILCA, respectively. The intrinsic scatter is constrained with upper limits of $\sigma_{\ln Y} < 0.12$ (NILC) and $\sigma_{\ln Y} < 0.16$ (MILCA).

The *Planck* SZ measurement for the merging clusters is in overall agreement with the scaling relation. We repeat the linear regression for the full sample, and find that the results do not significantly change; $\alpha = 1.51_{-0.23}^{+0.27}$, $\sigma_{\ln Y} < 0.24$ (NICL) and $\alpha = 1.59_{-0.22}^{+0.28}$, $\sigma_{\ln Y} < 0.16$ (MILCA). The deviations from the best-fit scaling relation is discussed in detail later.

Planck Collaboration et al. (2016) have computed the stacked Y_{SZ} around optically-selected clusters from the SDSS III (Wen et al. 2012). Through the scaling-relation between the richness and mass for a subsample of galaxy clusters, they obtain the power-law slope, $\alpha = 1.92 \pm 0.42$ in the $Y_{\text{SZ}} - M_{200}$ relation, although the assumed functional form of the scaling relation is $Y_{\text{SZ}}E(z)^{-2/3} \propto M^\alpha$ is different from ours. A fair comparison of the normalization is very difficult because of the different choices of the measurement radius and the adopted scaling relation. Furthermore, their mass calibration is not carried out consistently for the whole sample clusters in contrast to our method. As the zero-th order comparison, we obtain $Y_0 \sim 4 \times 10^{-6}$ [Mpc²] in our definition from their values. Therefore, their measurements does not necessarily conflict with our results.

We next compute the stacked X-ray luminosity from the RASS in the energy band of 0.1 – 2.4 keV. The X-ray luminosity scales as $L_X \propto \rho_{\text{gas}}^2 V \Lambda(T_X)$ by thermal bremsstrahlung emission, where ρ_{gas} is the gas mass density and Λ is the emissivity. Since the emissivity is almost constant in the soft band, the scaling relation between the X-ray luminosity and cluster mass have the form of

$$L_X^{\text{RASS}} E(z)^{-1} \propto M_{200}E(z), \quad (15)$$

under an assumption of constant gas mass fraction. However, we find that our result prefers a steeper slope (the right panel of Fig. 7). When we fit the scaling relation for the single clusters with a free slope,

$$L_X E(z)^{-1} = L_0 \left(\frac{M_{200}E(z)}{M_0} \right)^\alpha, \quad (16)$$

we obtain $\alpha = 1.58_{-0.30}^{+0.36}$ and $L_0 = 4.93_{-1.66}^{+2.01} \times 10^{42}$ [ergs⁻¹]. We obtain the constraint on the log-normal scatter of L_X as

$\ln \sigma_L < 0.21$, which is slightly larger than that of Y_{SZ} . We re-fit including the merging clusters, and find $L_0 = 4.46_{-1.50}^{+1.96} \times 10^{42}$ [ergs⁻¹], $\alpha = 1.79_{-0.30}^{+0.35}$ and $\ln \sigma_L < 0.29$. The slope is slightly steeper and intrinsic scatter is larger, albeit consistent within 1σ errors.

Rykoff et al. (2008) studied the scaling relation between the X-ray luminosity in 0.1-2.4 keV and the total mass for the maxBCG galaxy clusters (Koester et al. 2007) in the redshift range $0.1 \leq z \leq 0.3$. They find $\alpha = 1.65 \pm 0.13$ and $L_0 = 3.4 \pm 0.4(\text{stat}) \pm 0.4(\text{sys}) 10^{42}$ [ergs⁻¹], which are in agreement with our results. Anderson et al. (2015) measured the stack X-ray emission around locally brightest galaxies from the SDSS, using the RASS data. They measure X-ray luminosity in 0.5 – 2.0 keV and study a scaling relation assuming $L_X \propto E(z)^{7/3} M_{500}^\alpha$, where the mass M_{500} is estimated by their internal technique. They obtain a steep slope, $\alpha = 1.85_{-0.16}^{+0.15}$, which is in good agreement with our results. We convert the normalization from their scaling relation to ours, taking into account the difference of the energy band and $M_{500} = 0.64 M_{200}$ based on our weak-lensing measurement. The resulting normalization, $L_0 \sim 4.4 \times 10^{42}$ ergs⁻¹, is in a good agreement with ours. Arnaud et al. (2010) studied the L_X and mass scaling relation, at the overdensity 500, for a representative sample of 33 X-ray clusters from the REFLEX catalogue (Böhringer et al. 2007). The best-fit slope for X-ray selected clusters, $\alpha = 1.64$, is consistent with that of the optically selected clusters. We convert the X-ray luminosity from within r_{500} to within r_{200} using $L_{500}/L_{200} = 0.96$ (Piffaretti et al. 2011). The resulting normalization is $L_0 = 1.5 \times 10^{43}$, ergs⁻¹, which is about two times higher than that for the CAMIRA clusters. Similar results are found in shear-selected clusters. Miyazaki et al. (2018a) found that the X-ray luminosity for the shear-selected clusters is about half of that of X-ray clusters drawn from the MCXC clusters (Piffaretti et al. 2011), using the same selection criteria on the mass and redshift.

We next study the difference of the scaling relations between the merging and single cluster samples. In order to discuss the deviation of the scaling relation due to the merging phenomena, we consider an ideal case that the two clusters of which mass and SZ or X-ray observables of two merging clusters perfectly follow scaling relations, $X = g(M) \equiv AM^\alpha$, where $M = M_{200}E(z)$ and $X = Y_{\text{SZ}}E(z)$ or $X = L_X E(z)^{-1}$ in this study. If X for the two clusters is conserved during mergers or by the projection effect, the total X_{tot} measured within a certain radius can be derived by

$$X_{\text{tot}} = X_1 + X_2 = A \frac{1 + (M_2/M_1)^\alpha}{(1 + M_2/M_1)^\alpha} (M_1 + M_2)^\alpha, \quad (17)$$

where the subscripts (1 and 2) label two clusters. Therefore, after the merger or the projection, X is deviated by a factor of $f_M = (1 + (M_2/M_1)^\alpha)/(1 + M_2/M_1)^\alpha$ from the scaling relation. Since our sample is contaminated by the projec-

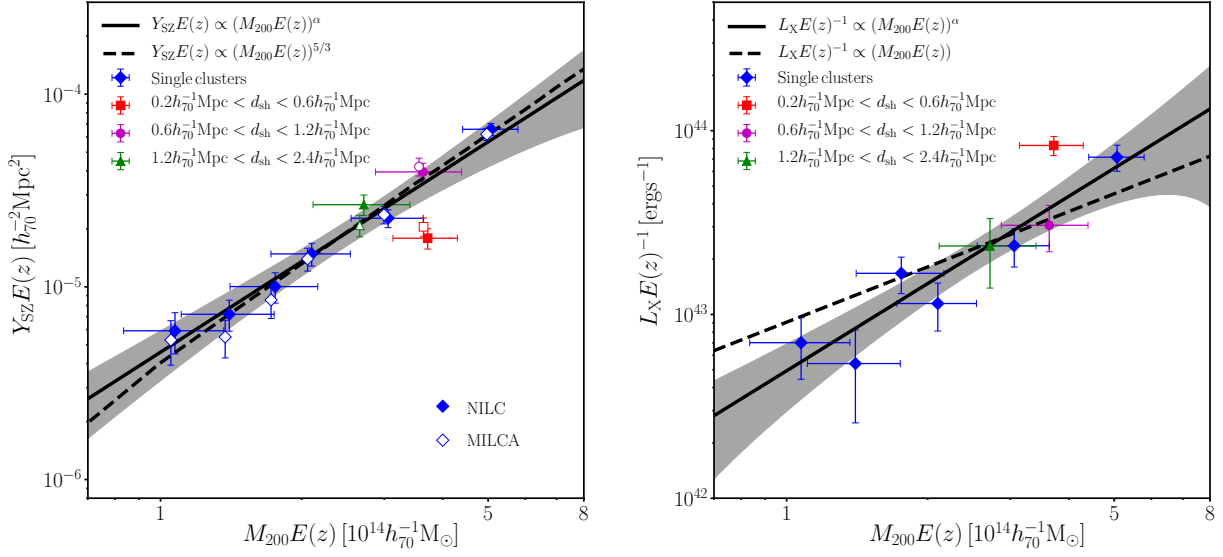


Fig. 7. *Left:* The *Planck* Y_{SZ} and M_{200} scaling relation. Blue diamonds denote the single clusters. Red square, magenta circle, and green triangle are the merging clusters divided by peak separations. The solid and open symbols are NILC and MILCA data, respectively. The solid and gray area denote the best-fit and its 1σ error of the scaling relation for the single clusters with a free slope. The dashed line is the best-fit of the scaling relation with a fixed slope. *Right:* Similar to the left panel, but for the *ROSAT* L_X and M_{200} scaling relation.

tion effect, we adopt a statistical treatment in order to quantify the merger boost on the SZ and X-ray observables. Based on the projected number density of the subhalos (Sec. 3.3), a chance probability of the projection effect for each cluster in our sample can be calculated by integrating $\Sigma_{\text{proj}}^{(n)}$ from the innermost to outermost radii on the sky; $P_{\text{proj}} = 0.046_{-0.026}^{+0.023}$ for $0.2 - 0.6h_{70}^{-1}$ Mpc, $P_{\text{proj}} = 0.154_{-0.088}^{+0.079}$ for $0.6 - 1.2h_{70}^{-1}$ Mpc, and $P_{\text{proj}} = 0.614_{-0.353}^{+0.314}$ for $1.2 - 2.4h_{70}^{-1}$ Mpc, respectively. We here introduce the boost factor of b_X of the ICM, caused by cluster mergers, in the scaling relation. The scaling relation can be statistically expressed by

$$X_{\text{tot}} = Ab_X f_M M_{\text{tot}}^\alpha (1 - P_{\text{proj}}) + Af_M M_{\text{tot}}^\alpha P_{\text{proj}}. \quad (18)$$

Consequently, the boost factor of cluster mergers is obtained by

$$b_X = \frac{X/g(M) - f_M P_{\text{proj}}}{f_M (1 - P_{\text{proj}})}. \quad (19)$$

If b_X is higher than unity, the gas observables are enhanced by cluster mergers.

Fig. 8 shows the resulting boost factors of Y_{SZ} and L_X . We use the NICL Y_{SZ} scaling relation. We adopt the best-fit scaling relations with free slopes. The measurement errors of weak-lensing masses, the cluster mass ratios and the probability of the projection effect are all taken into account. Therefore, the errors become larger than those in Figure 7. Especially, the large error for clusters at $1.2 - 2.4h_{70}^{-1}$ is attributed to the error of the probability of the projection effect. The boost factors of all the single clusters and the merging clusters with peak separations of $1.2 - 2.4h_{70}^{-1}$ Mpc are consistent with unity. Hence,

once the projection effect is corrected, the scaling relation holds for the merging clusters when the subcluster is located outside the main cluster. On the other hand, the merging clusters with $0.2 - 0.6h_{70}^{-1}$ Mpc and $0.6 - 1.2h_{70}^{-1}$ Mpc show $b_L > 1$ and $b_Y > 1$, respectively, albeit with a low statistical significance level. Interestingly, the boost factors in the other scaling relations are $b_Y \sim 1$ at $0.2 - 0.6h_{70}^{-1}$ Mpc and $b_L \sim 1$ at $0.6 - 1.2h_{70}^{-1}$ Mpc, respectively. This feature statistically implies that the electron number density and the electron temperature is enhanced in each subsample of at $0.2 - 0.6h_{70}^{-1}$ Mpc and $0.6 - 1.2h_{70}^{-1}$ Mpc, respectively. Since the scaling relation we discuss here is based on the stacked quantities, it does not always indicate that all the clusters in the subsamples are affected by the merger boost. Since each subsample contains clusters both before and after core passages, we cannot discuss individual boost factors without knowing the fraction of clusters before and after core passages. Future systematic X-ray and SZE observations with high angular resolutions are essential for understanding gas physics involved in cluster mergers. The follow-up X-ray and SZE observations will enable us to carry out individual cluster analysis and investigate the merger boost in scaling relations based on individual measurements.

Krause et al. (2012) found in cosmological simulations that major mergers within a Gyr timescale cause an asymmetric scatter in the Y_{SZ} scaling relation so that the inferred mass of merging systems is biased low. They also found that clusters with lower concentration parameters have a trend to have lower Y_{SZ} at fixed masses. The trend conflicts with our results (Figs 2 and

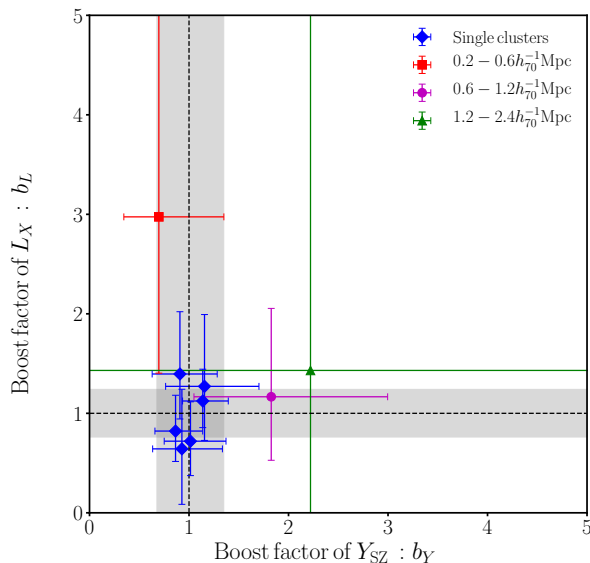


Fig. 8. Boost factors of Y_{SZ} and L_X caused by cluster mergers. Point symbols are the same as in Fig. 7. The gray areas denote the regions combined with the 1σ uncertainty of the normalization and the upper limit of the intrinsic scatter. The boost factors of the merging clusters with peak separations of $0.2 - 0.6h_{70}^{-1}$ Mpc and $0.6 - 1.2h_{70}^{-1}$ Mpc are higher than unity, in the L_X and Y_{SZ} directions, respectively.

8). Shaw et al. (2008) pointed out, using adiabatic simulations, a positive correlation between the scatter in concentration and integrated Y parameter. Yu et al. (2015) reported that the shock propagates out to $\sim r_{200}$ after a few Gyr from the closest encounter and the energy from random gas motions decays into thermal energy over the next few Gyr. Consequently, the thermal Y_{SZ} within r_{200} increase by $\sim 8\%$. Although a fair comparison with their results is difficult, the trend is likely to be different from our results. Therefore, future individual cluster analyses for our sample of the merging clusters are essential to understand more precisely the merger boost and its merger-phase dependence.

3.7 Non-detection of diffuse radio emissions and collision velocities

It is well known that major mergers host diffuse radio synchrotron emission, the so-called radio halos and relics (e.g. Roettiger et al. 1999; Govoni et al. 2004; Venturi et al. 2007, 2008; van Weeren et al. 2010, 2011; Feretti et al. 2012). The radio halos are diffuse radio emission around cluster centers and relics are filamentary radio emission at cluster outskirts. We search diffuse radio emissions in archival NVSS (1.4 GHz; Condon et al. 1998) and TGSS (147.5 MHz; Intema et al. 2017) data. Following de Gasperin et al. (2018), we computed spectral index maps by matching pixel-by-pixel NVSS and beam-size-matched TGSS maps. Here, we convolve the TGSS images with

a circular beam with the size same as that the NVSS because of the lower resolution of NVSS. The background rms noise of the NVSS is nearly uniform at $0.45 \text{ mJybeam}^{-1}$. The rms noise of the TGSS are locally estimated by 4σ clippings. The typical rms is $\sim 3 \text{ mJybeam}^{-1}$. de Gasperin et al. (2018) discovered the following feature; spectral index maps of radio lobes associated with AGNs show steeper values at its outer edges than at around its peaks. On the other hand, the spectral index gradient of radio relics is expected to be along the minor axis of the filamentary structure. We cross-match the spectral index map and HSC galaxy maps to identify radio halos and relics. We also compare the NVSS and TGSS radio images with the HSC optical images for an assessment of whether the radio sources are associated with optical galaxies or not. However, we do not find any strong candidates of radio relics and halos in our sample. Almost all radio sources turn out to be associated with member galaxies or high redshift sources.

We discuss the non-detection of radio relics and halos from a viewpoint of the merger collision velocity. We compare collision velocities of the optical subhalos with shock velocities in merging clusters hosting diffuse radio emission. We assume $\sqrt{3}v_{\text{los}}$ as the collision velocity of the subhalos, where v_{los} is the line-of-sight velocity estimated by matching SDSS spectroscopic redshifts (Sec. 3.2). The shock velocities in massive merging clusters are measured by temperature jumps found in X-ray observations (Markevitch 2006; Russell et al. 2011, 2012; Akamatsu & Kawahara 2013; Akamatsu et al. 2013; Owers et al. 2014; Eckert et al. 2016; Dasadia et al. 2016; Sarazin et al. 2016; Emery et al. 2017). The shock features are associated with diffuse radio emission. We assume based on the X-ray morphology that the shock is moving on the sky plane. The probability density function (PDF) of collision velocities is shown in Fig. 9. Since the measurement uncertainty of X-ray shock velocity is relatively large, the mean values and error bars of shock velocity in each bin are computed from 10000 Monte Carlo redistributions. The PDF of collision velocities of the optically-defined mergers are systematically lower than that of the merging clusters with diffuse radio emissions. The modes of the collision velocity PDFs differ by a factor of 2.5, indicating that the kinetic energy of the optically-defined mergers is about one order of magnitude lower than that of the merging clusters with diffuse radio emissions. Assuming a constant conversion from the kinetic energy of cluster mergers to a synchrotron radio power, the radio power for optically-defined mergers is expected to be one order of magnitude lower than the observed values of the radio sources. It is thus very difficult to detect diffuse radio emission in our sample in the archival radio data. The future joint search with the LOFAR Two-metre Sky Survey (LoTSS Shimwell et al. 2017, 2018) would be powerful to search diffuse radio emissions in the merging clusters with the better sensitivity and higher resolution. The low-

frequency radio telescopes like LOFAR, Murchison Widefield Array (MWA), the Australian SKA Pathfinder (ASKAP), and Square Kilometre Array (SKA) will be able to search diffuse radio emission from relativistic electrons with long lifetimes in merging clusters.

We compare our result with the PDF of the pairwise velocity of cluster mergers in cosmological simulations (Bouillot et al. 2015). The solid black line in Fig. 9 is the PDF at $z = 0.5$ retrieved from Fig. 12. of Bouillot et al. (2015). The selection criteria are halo pairs with average mass $M > 10^{14} h^{-1} M_{\odot}$ and distance separations $< 10 h^{-1} \text{Mpc}$ with ΛCDM cosmology, which is similar to our sample selection. The predicted PDF agrees well with our results. Similar results are also reported by studies of numerical simulations (e.g. Lee & Komatsu 2010; Thompson & Nagamine 2012; Kraljic & Sarkar 2015). Thompson & Nagamine (2012) showed that the pair population at a high end of the pairwise velocity distribution decreases with smaller separations. Specifically, pairs with separations $< 2 h^{-1} \text{Mpc}$ have the maximum pairwise velocity on the order of $\sim 1800 \text{kms}^{-1}$ at $z \sim 0.3 - 0.5$. However, since the number density of the pairwise velocity at $v \gtrsim 2000 \text{kms}^{-1}$ is two orders of magnitude lower than that of $v \lesssim 1000 \text{kms}^{-1}$, the theoretical prediction in the high probability velocity range is not significantly changed by a different choice of distance separations. In contrast to the good agreement between the predicted and observed subhalo velocities, the shock velocity in the merging clusters with diffuse radio emissions is systematically higher. One of differences between the two observing samples is the mass; our sample of clusters has a moderate mass $M_{200} \sim 3 \times 10^{14} h_{70}^{-1} M_{\odot}$, whereas the merging clusters hosting diffuse radio emissions are more massive (e.g. $\sim 10^{15} h_{70}^{-1} M_{\odot}$; Okabe et al. 2015). Kraljic & Sarkar (2015) showed that the fraction of halo pairs with higher relative velocities is larger for massive halos. A large number of pairs with masses larger than $\sim 10^{15} h^{-1} M_{\odot}$ and relative velocities $\gtrsim 2000 \text{kms}^{-1}$ are also found in Bouillot et al. (2015). Therefore, the discrepancy between the shock and subhalo velocity distributions can be explained by a selection bias. In other words, the merging clusters with diffuse radio emission have high collision velocities.

3.8 Stacked images of low redshift and massive clusters

We compute stacked images, by aligning the main-subhalo pairs, of luminous red galaxies, mass, RASS X-ray, *Planck* SZE, NVSS radio at 1.4 GHz and TGSS radio at 147 MHz, in order to understand the interplay between the baryonic components and dark matter during cluster mergers. Since the empirical FWHM of the RASS image tracing the gas density is ~ 3.3 arcmin, gas structures of low redshift and massive clusters can be resolved. We therefore select 36 low redshift and massive

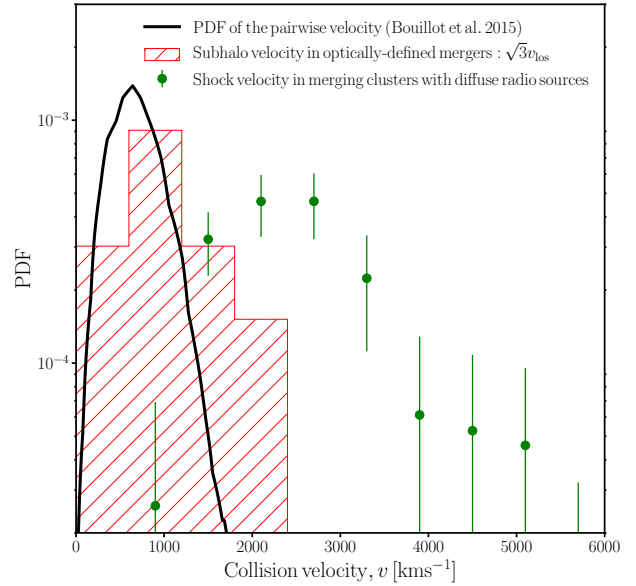


Fig. 9. The probability density function (PDF) of collision velocities of cluster mergers. The hatched red histogram shows the PDF of $\sqrt{3}$ -times line-of-sight velocities of the optically-defined subhalos. The green circles are the PDF of shock velocities of the ICM in merging clusters associated with diffuse radio emission. The black solid line is a theoretical prediction of the pairwise velocity PDF calculated from numerical simulations (Bouillot et al. 2015).

clusters from the merging clusters, using the selection criteria of $z < 0.4$ and $N_{\text{cor}} > 30$. The number of sampling clusters is comparable to the minimum number of the subsamples in the scaling relation study (Sec. 3.6 and table 1). The maps are rotated such that the cluster and subhalo pair are aligned with the x -axis in the images, with the center of the main peaks, and then rescaled according to their corresponding angular pair separation. We denote the x -axis as the merger axis. We excluded known point sources for the X-ray and SZE maps as in the scaling relation study. As for the NVSS and TGSS images, we do not apply exclude any point sources or extended radio lobes to avoid artifact features. In the X-ray and radio bands, we consider the changes of the beam (FWHM) sizes of each cluster image, caused by the rotations and rescalings. The resulting FWHMs are shown as the black circle at the bottom-left corner of each panel of Fig. 10. For a visualization purpose, we do not adopt the weight of lensing contribution in each map making.

The top-left and top-right panels show the number distribution of luminous red galaxies and the weak lensing mass map, respectively. The distribution of red galaxies is concentrated around the main and sub peaks as expected. The weak-lensing mass map shows two peaks associated with the galaxy peaks and an elongated distribution bridging between them. The peak-height ratio between the sub and main halos in the mass map is ~ 0.5 , slightly lower than that in the galaxy map, ~ 0.8 .

The middle-left and middle-right panels are stacked RASS

X-ray and *Planck* SZE maps, respectively. The X-ray main and second peaks are associated with the main and subhalos, respectively. The X-ray flux from the subhalo peak is much smaller than from the main halo peak, indicating that the gas halo associated with the subhalo is disrupted by ram-stripping and/or hydrodynamic instabilities. The peak position of the second X-ray peak is slightly offset from the subhalo center to the main peak. Although the trend is not significant, it implies a presence of ram pressure stripping and that some fraction of the subsample is at the post merger phase. The central core of X-ray emission is elongated along the merger axis, whereas the overall distribution is oriented almost perpendicular to the merger axis. To quantify the ellipticity, we fit the two dimensional distribution with an elliptical β model convoluted with the PSF size. The orientation angle of the major axis of the central gas core is $\phi_e = 3_{-16}^{+14}$ deg from the merger axis. On the other hand, the major axis of the overall distribution is $\phi_e = 61_{-4}^{+5}$ deg from the merger axis. When the image of each cluster is randomly rotated centering the main peak, the feature disappears. We also compute the stacked images for the subsamples divided by peak separations. We found that the elongated gas perpendicular to the merger axis is significant in the merging clusters with $0.2h_{70}^{-1} \text{ Mpc} < d_{\text{sh}} < 0.6h_{70}^{-1} \text{ Mpc}$. The asymmetrical distribution suggests that, as the two gas cores are approaching, the main gas core is stretched along the merger axis, but the gas halo outside the core is compressed along the merger axis, and subsequently pushed outwards perpendicular to the axis (Ricker & Sarazin 2001; ZuHone 2011; Ha et al. 2018). The expansion is significant after the core passage, which is also consistent with the offset feature between galaxy and gas due to ram-pressure stripping. If there is non-zero spin-parameter, the direction of the expansion is slightly shifted (e.g. Ricker & Sarazin 2001). Although the elongation feature of main gas cores along the merger axis and the destruction of gas subhalos were reported in on-going mergers by X-ray and weak-lensing joint analyses (e.g. Okabe & Umetsu 2008; Okabe et al. 2011, 2015; Medezinski et al. 2015), the expanding feature perpendicular to the merger axis is not reported elsewhere. A caveat is that the optically-defined merging clusters cannot distinguish between pre- and post- merger phase. Nevertheless, high X-ray luminosity is found in the closest-separation merging clusters at $0.2h_{70}^{-1} \text{ Mpc} < d_{\text{sh}} < 0.6h_{70}^{-1} \text{ Mpc}$ (Fig. 7). The overall distribution of the stacked *Planck* SZE map is similar to the X-ray distribution. Since the *Planck* FWHM is much poorer than the RASS one, we cannot constrain the major axis of the gas halo ellipticity. Although the stacked images suggest that the post-merging clusters are dominant in the low redshift and massive clusters, future systematic observations by *XMM-Newton*, *eROSITA*, *Chandra*, and ActPol with high angular resolutions will be crucial to identify cluster dynamical state of each cluster and reveal how gas features are changed by their merging phase.

The bottom panels show the stacked NVSS and TGSS images. Very significant radio emissions ($> 10\sigma_{\text{rms}}$) are found around the main and sub peaks. The spectral index estimated from the two images is ~ -1 . They are radio lobes associated with cluster galaxies. In the NVSS band, the extended radio distribution at several σ_{rms} is found between the two peaks. However, since these radio lobes are too bright, less significant radio emissions are hindered by envelopes of radio lobes, and therefore we cannot identify other diffuse emission at outer radii.

4 Summary

We carried out multi-wavelength studies of optically-defined merging clusters selected from the Hyper Suprime-Cam Subaru Strategic Program. We adopted a peak-finding method of projected distributions of luminous red galaxies, and defined merging clusters with multiple-peaks and single clusters with single peak from the HSC CAMIRA cluster catalog. Since the number of luminous red galaxies is almost conserved during cluster mergers, in contrast to a merging cluster catalog in X-ray that is significantly affected by the merger boost, our catalog represents a homogeneous, unbiased sample of cluster mergers. Our main results are summarized as follows.

- Our weak lensing analysis has shown that halo concentration for the merging clusters is $\sim 70\%$ smaller than that of the single clusters. The low concentration is in good agreement with predictions of numerical simulations (e.g. Neto et al. 2007; Child et al. 2018). The concentration parameter decreases as the subhalo distance increases within r_{200} .
- We also conducted a two-halo component analysis to interpret the stacked tangential shear profile and found that the subhalo mass ratio to the main halo mass is $\gtrsim 0.1$. Once the subhalo component is modeled separately, the concentration of the main halos of the merging clusters is consistent with that of the single clusters.
- The spatial distribution of subhalos is found to be less centrally concentrated than the dark matter distribution of the main halo, which agrees with theoretical predictions considering dynamical friction and tidal stripping of subhalos (e.g. Gao et al. 2004; Diemand et al. 2004; Han et al. 2016). We found that the chance probability of the projection effect of surrounding clusters along the line-of-sight is not large at $r \lesssim r_{200}$.
- Using the SDSS spectroscopic data, we have shown that most of the subhalos are located within the caustics boundary in the stacked velocity-space diagram.
- We estimated red fractions of cluster galaxies based on photometric redshifts, and found that the red fractions of the merging clusters are comparable to or smaller than those of the single clusters.

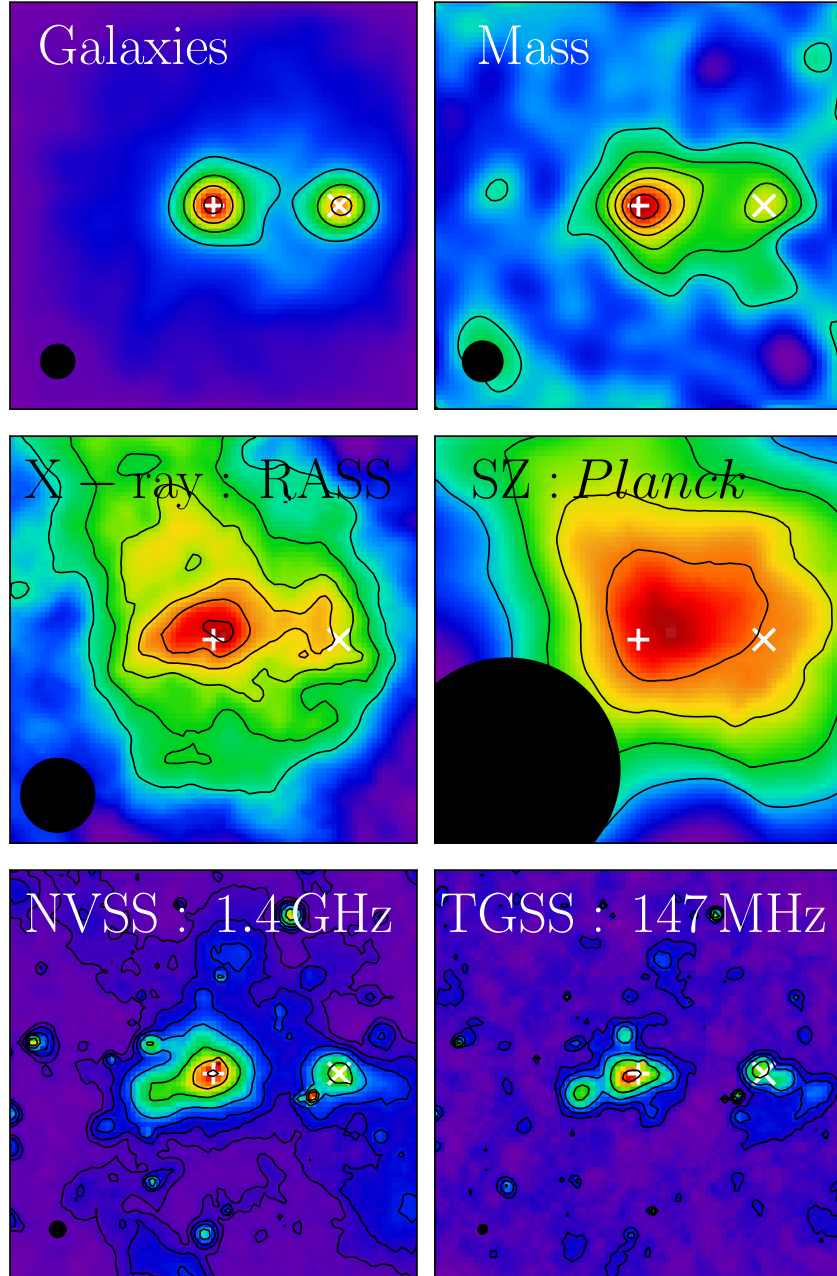


Fig. 10. Stacked X-ray images (count s^{-1}) for 36 merging clusters with $z < 0.4$ and $N_{\text{cor}} > 30$. The x-axis is the merger axis. The white plus and cross are the positions of the highest and second highest peaks in galaxy maps. The black circle (elliptical) at the bottom-left corner of each panel denotes FWHM of each stacked image. *Top-left:* The number distribution of luminous red galaxies. Overlaid are contours more than 3 galaxies per pixel, stepped by 2 galaxies. Two galaxy concentrations are found around the main cluster center and the subhalo. *Top-right:* The weak lensing mass map. Overlaid are contours more than 1σ , stepped by 2σ . Here, σ is the 1σ uncertainty of the weak-mass reconstruction. *Middle-left:* The RASS X-ray map. Overlaid are contours more than 2σ , stepped by 1σ , where σ is the noise of the stacked map. The central gas distribution is elongated along the merger axis, whereas the overall gas is oriented almost perpendicular to the merger axis. *Middle-right:* The *Planck* SZ map. Overlaid are contours more than 5σ , stepped by 2σ . Here, σ denotes the noise of stacked y map. *Bottom-left:* The NVSS radio map (1.4 GHz) Overlaid are contours are $[2,5,10,20,40,60,80] \times \sigma_{\text{rms}}$, where σ_{rms} is the root mean square (rms) noise in the stacked NVSS map. *Bottom-right:* The TGSS radio map (147.5 MHz) Overlaid are contours are $[2,5,10,20,40] \times \sigma_{\text{rms}}$, where σ_{rms} is the rms noise in the stacked TGSS map. We do exclude point sources in X-ray and SZE measurements but do not exclude radio point sources to avoid artifact features.

- We found the tight correlation between the mass and richness and no significant deviation of the merging clusters.
- We derived scaling relations of the *Planck* SZE (Y_{SZ}) and *ROSAT* X-ray luminosity (L_X) with masses and found that their slopes are consistent with and steeper than self-similar solutions, respectively. We estimated the merger boosts on Y_{SZ} and L_X taking account of the mass ratio of the main and sub clusters and the projection effect. The boost factors of L_X and Y_{SZ} are found to be about a factor of two for the merging clusters at $0.2 - 0.6 h_{70}^{-1}$ Mpc and $0.6 - 1.2 h_{70}^{-1}$ Mpc, respectively.
- We did not find strong candidates of radio halos and relics in our merging cluster sample.
- The histogram of collision velocities of our samples is in good agreement with cosmological simulations (e.g. Bouillot et al. 2015) and ~ 2.5 times lower than shock velocities of major mergers with diffuse radio emission.
- The RASS X-ray stacked image, aligned with the main-subhalo pairs, for low redshift and massive clusters, shows that the central gas core is elongated along the merger axis and overall gas distribution is misaligned by ~ 60 deg. The *Planck* SZE map with poor angular resolution shows the similar elongation. The feature indicates that the ICM at large radii are pushed outwards by colliding two clusters.

Cross-matching our merging cluster sample with the ongoing and future surveys (*eROSITA*, ACTPol, and LoTSS) and follow-up X-ray, radio, and spectroscopic observations of merging clusters at various merging phases will be crucial to understand the interplay between baryons and dark matter over the whole process of cluster mergers and constrain the merger boost more precisely. Especially, individual cluster analyses will be able to identify merger phases and their multi-wavelength studies will prove their dynamical dependence underlying cluster mergers.

Current peak-finding method cannot resolve a transient state of pericenter of subhalo (e.g. Ludlow et al. 2012) due to the limitation of smoothing scale. Further improvement of techniques to find merging clusters from sparse distributions of member galaxies is vitally important.

Acknowledgments

The Hyper Suprime-Cam (HSC) collaboration includes the astronomical communities of Japan and Taiwan, and Princeton University. The HSC instrumentation and software were developed by the National Astronomical Observatory of Japan (NAOJ), the Kavli Institute for the Physics and Mathematics of the Universe (Kavli IPMU), the University of Tokyo, the High Energy Accelerator Research Organization (KEK), the Academia Sinica Institute for Astronomy and Astrophysics in Taiwan (ASIAA), and Princeton University. Funding was contributed by the FIRST program from Japanese Cabinet Office, the Ministry of Education, Culture, Sports, Science and Technology (MEXT), the Japan Society for the Promotion of Science (JSPS), Japan Science and Technology Agency (JST), the Toray

Science Foundation, NAOJ, Kavli IPMU, KEK, ASIAA, and Princeton University.

This paper makes use of software developed for the Large Synoptic Survey Telescope. We thank the LSST Project for making their code available as free software at <http://dm.lsst.org>.

The Pan-STARRS1 Surveys (PS1) have been made possible through contributions of the Institute for Astronomy, the University of Hawaii, the Pan-STARRS Project Office, the Max-Planck Society and its participating institutes, the Max Planck Institute for Astronomy, Heidelberg and the Max Planck Institute for Extraterrestrial Physics, Garching, The Johns Hopkins University, Durham University, the University of Edinburgh, Queens University Belfast, the Harvard-Smithsonian Center for Astrophysics, the Las Cumbres Observatory Global Telescope Network Incorporated, the National Central University of Taiwan, the Space Telescope Science Institute, the National Aeronautics and Space Administration under Grant No. NNX08AR22G issued through the Planetary Science Division of the NASA Science Mission Directorate, the National Science Foundation under Grant No. AST-1238877, the University of Maryland, and Eotvos Lorand University (ELTE) and the Los Alamos National Laboratory.

Based on data collected at the Subaru Telescope and retrieved from the HSC data archive system, which is operated by Subaru Telescope and Astronomy Data Center at National Astronomical Observatory of Japan.

This work was supported by the Funds for the Development of Human Resources in Science and Technology under MEXT, Japan and Core Research for Energetic Universe in Hiroshima University (the MEXT program for promoting the enhancement of research universities, Japan).

M.O. is supported in part by World Premier International Research Center Initiative (WPI Initiative), MEXT, Japan, and JSPS KAKENHI Grant Number JP15H05892 and JP18K03693. H.A acknowledges the support of NWO via a Veni grant. SRON is supported financially by NWO, the Netherlands Organization for Scientific Research.

References

- Abolfathi, B., Aguado, D. S., Aguilar, G., et al. 2018, *ApJS*, 235, 42
- Aihara, H., Armstrong, R., Bickerton, S., et al. 2018a, *PASJ*, 70, S8
- Aihara, H., Arimoto, N., Armstrong, R., et al. 2018b, *PASJ*, 70, S4
- Akamatsu, H., Inoue, S., Sato, T., et al. 2013, *PASJ*, 65, 89
- Akamatsu, H., & Kawahara, H. 2013, *Publications of the Astronomical Society of Japan*, 65, 16
- Akamatsu, H., Gu, L., Shimwell, T. W., et al. 2016, *A&A*, 593, L7
- Akamatsu, H., Mizuno, M., Ota, N., et al. 2017, *A&A*, 600, A100
- Anderson, M. E., Gaspari, M., White, S. D. M., Wang, W., & Dai, X. 2015, *MNRAS*, 449, 3806
- Arnaud, M., Pratt, G. W., Piffaretti, R., et al. 2010, *A&A*, 517, A92
- Bekki, K. 1999, *ApJ*, 510, L15
- Belsole, E., Pratt, G. W., Sauvageot, J.-L., & Bourdin, H. 2004, *A&A*, 415, 821
- Bhattacharya, S., Habib, S., Heitmann, K., & Vikhlinin, A. 2013, *ApJ*, 766, 32
- Böhringer, H., Schuecker, P., Pratt, G. W., et al. 2007, *A&A*, 469, 363
- Boller, T., Freyberg, M. J., Trümper, J., et al. 2016, *A&A*, 588, A103
- Bosch, J., Armstrong, R., Bickerton, S., et al. 2018, *PASJ*, 70, S5
- Bouillot, V. R., Alimi, J.-M., Corasaniti, P.-S., & Rasera, Y. 2015, *MNRAS*, 450, 145
- Brunetti, G., Giacintucci, S., Cassano, R., et al. 2008, *Nature*, 455, 944
- Bullock, J. S., Kolatt, T. S., Sigad, Y., et al. 2001, *MNRAS*, 321, 559
- Butcher, H., & Oemler, Jr., A. 1984, *ApJ*, 285, 426

- Carrasco Kind, M., & Brunner, R. J. 2014, *MNRAS*, 438, 3409
- Child, H. L., Habib, S., Heitmann, K., et al. 2018, *ApJ*, 859, 55
- Cibirka, N., Cypriano, E. S., Brimiouille, F., et al. 2017, *MNRAS*, 468, 1092
- Condon, J. J., Cotton, W. D., Greisen, E. W., et al. 1998, *AJ*, 115, 1693
- Coupon, J., Czakon, N., Bosch, J., et al. 2018, *PASJ*, 70, S7
- Dasadia, S., Sun, M., Sarazin, C., et al. 2016, *ApJ*, 820, L20
- de Gasperin, F., Intema, H. T., & Frail, D. A. 2018, *MNRAS*, 474, 5008
- Deshev, B., Finoguenov, A., Verdugo, M., et al. 2017, *A&A*, 607, A131
- Diaferio, A., & Geller, M. J. 1997, *ApJ*, 481, 633
- Diemand, J., Moore, B., & Stadel, J. 2004, *MNRAS*, 352, 535
- Diemer, B., & Kravtsov, A. V. 2015, *ApJ*, 799, 108
- Dressler, A., & Gunn, J. E. 1983, *ApJ*, 270, 7
- Duffy, A. R., Schaye, J., Kay, S. T., & Dalla Vecchia, C. 2008, *MNRAS*, 390, L64
- Eckert, D., Jauzac, M., Vazza, F., et al. 2016, *MNRAS*, 461, 1302
- Emery, D. L., Bogdán, Á., Kraft, R. P., et al. 2017, *ApJ*, 834, 159
- Evrard, A. E. 1991, *MNRAS*, 248, 8P
- Feretti, L., Giovannini, G., Govoni, F., & Murgia, M. 2012, *A&A Rev.*, 20, 54
- Ferrari, C., Benoist, C., Maurogordato, S., Cappi, A., & Slezak, E. 2005, *A&A*, 430, 19
- Fujita, Y., Takizawa, M., Nagashima, M., & Enoki, M. 1999, *PASJ*, 51, L1
- Fujita, Y., Takizawa, M., & Sarazin, C. L. 2003, *ApJ*, 584, 190
- Fujita, Y., Takizawa, M., Yamazaki, R., Akamatsu, H., & Ohno, H. 2015, *ApJ*, 815, 116
- Furusawa, H., Koike, M., Takata, T., et al. 2018, *PASJ*, 70, S3
- Gao, L., White, S. D. M., Jenkins, A., Stoehr, F., & Springel, V. 2004, *MNRAS*, 355, 819
- Górski, K. M., Hivon, E., Banday, A. J., et al. 2005, *ApJ*, 622, 759
- Govoni, F., Markevitch, M., Vikhlinin, A., et al. 2004, *ApJ*, 605, 695
- Ha, J.-H., Ryu, D., & Kang, H. 2018, *ApJ*, 857, 26
- Han, J., Cole, S., Frenk, C. S., & Jing, Y. 2016, *MNRAS*, 457, 1208
- Hirata, C., & Seljak, U. 2003, *MNRAS*, 343, 459
- Huang, S., Leauthaud, A., Murata, R., et al. 2018, *PASJ*, 70, S6
- Hurier, G., Macías-Pérez, J. F., & Hildebrandt, S. 2013, *A&A*, 558, A118
- Intema, H. T., Jagannathan, P., Mooley, K. P., & Frail, D. A. 2017, *A&A*, 598, A78
- Johnston, D. E., Sheldon, E. S., Wechsler, R. H., et al. 2007, *ArXiv e-prints*, 0709.1159
- Kaiser, N. 1987, *MNRAS*, 227, 1
- Kapferer, W., Ferrari, C., Domainko, W., et al. 2006, *A&A*, 447, 827
- Kawanomoto, S., Uruguchi, F., Komiyama, Y., et al. 2018, *PASJ*, 70, 66
- Kay, S. T., Peel, M. W., Short, C. J., et al. 2012, *MNRAS*, 422, 1999
- Koester, B. P., McKay, T. A., Annis, J., et al. 2007, *ApJ*, 660, 239
- Komiyama, Y., Chiba, M., Tanaka, M., et al. 2018, *ApJ*, 853, 29
- Koyama, Y., Kodama, T., Shimasaku, K., et al. 2010, *MNRAS*, 403, 1611
- Kraljic, D., & Sarkar, S. 2015, *J. Cosmology Astropart. Phys.*, 4, 050
- Krause, E., Pierpaoli, E., Dolag, K., & Borgani, S. 2012, *MNRAS*, 419, 1766
- Kronberger, T., Kapferer, W., Ferrari, C., Unterguggenberger, S., & Schindler, S. 2008, *A&A*, 481, 337
- Lavery, R. J., & Henry, J. P. 1988, *ApJ*, 330, 596
- Lee, J., & Komatsu, E. 2010, *ApJ*, 718, 60
- Ludlow, A. D., Navarro, J. F., Angulo, R. E., et al. 2014, *MNRAS*, 441, 378
- Ludlow, A. D., Navarro, J. F., Li, M., et al. 2012, *MNRAS*, 427, 1322
- Ludlow, A. D., Navarro, J. F., Springel, V., et al. 2009, *ApJ*, 692, 931
- Mamon, G. A., Biviano, A., & Boué, G. 2013, *MNRAS*, 429, 3079
- Mandelbaum, R., Seljak, U., Kauffmann, G., Hirata, C. M., & Brinkmann, J. 2006, *MNRAS*, 368, 715
- Mandelbaum, R., Lanusse, F., Leauthaud, A., et al. 2017, *arXiv:171000885*
- Mandelbaum, R., Miyatake, H., Hamana, T., et al. 2018, *PASJ*, 70, S25
- Markevitch, M. 2006, in *ESA Special Publication*, Vol. 604, *The X-ray Universe 2005*, ed. A. Wilson, 723
- Medezinski, E., Umetsu, K., Okabe, N., et al. 2015, *ArXiv e-prints*
- Medezinski, E., Oguri, M., Nishizawa, A. J., et al. 2018, *PASJ*, 70, 30
- Meneghetti, M., Rasia, E., Vega, J., et al. 2014, *ArXiv e-prints*
- Merten, J., Meneghetti, M., Postman, M., et al. 2015, *ApJ*, 806, 4
- Miyaoka, K., Okabe, N., Kitaguchi, T., et al. 2018, *PASJ*, 70, S22
- Miyatake, H., Battaglia, N., Hilton, M., et al. 2018, *arXiv:1804.05873*
- Miyazaki, S., Oguri, M., Hamana, T., et al. 2015, *ApJ*, 807, 22
- . 2018a, *PASJ*, 70, S27
- Miyazaki, S., Komiyama, Y., Kawanomoto, S., et al. 2018b, *PASJ*, 70, S1
- . 2018c, *PASJ*, 70, S1
- Nagai, D., & Kravtsov, A. V. 2005, *ApJ*, 618, 557
- Navarro, J. F., Frenk, C. S., & White, S. D. M. 1996, *ApJ*, 462, 563
- Neto, A. F., Gao, L., Bett, P., et al. 2007, *MNRAS*, 381, 1450
- Nishizawa, A. J., Oguri, M., Oogi, T., et al. 2018, *PASJ*, 70, S24
- Oguri, M. 2014, *MNRAS*, 444, 147
- Oguri, M., Bayliss, M. B., Dahle, H., et al. 2012, *MNRAS*, 420, 3213
- Oguri, M., Lin, Y.-T., Lin, S.-C., et al. 2018, *PASJ*, 70, S20
- Okabe, N., Akamatsu, H., Kakuwa, J., et al. 2015, *PASJ*
- Okabe, N., Bourdin, H., Mazzotta, P., & Maurogordato, S. 2011, *ApJ*, 741, 116
- Okabe, N., Futamase, T., Kajisawa, M., & Kuroshima, R. 2014, *ApJ*, 784, 90
- Okabe, N., & Smith, G. P. 2016, *MNRAS*, 461, 3794
- Okabe, N., Smith, G. P., Umetsu, K., Takada, M., & Futamase, T. 2013, *ApJ*, 769, L35
- Okabe, N., & Umetsu, K. 2008, *PASJ*, 60, 345
- Okabe, N., Zhang, Y.-Y., Finoguenov, A., et al. 2010, *ApJ*, 721, 875
- Owers, M. S., Baldry, I. K., Bauer, A. E., et al. 2013, *ApJ*, 772, 104
- Owers, M. S., Nulsen, P. E. J., Couch, W. J., et al. 2014, *ApJ*, 780, 163
- Piffaretti, R., Arnaud, M., Pratt, G. W., Pointecouteau, E., & Melin, J.-B. 2011, *A&A*, 534, A109
- Planck Collaboration, Aghanim, N., Arnaud, M., et al. 2011, *A&A*, 536, A12
- . 2016, *A&A*, 594, A22
- Ragagnin, A., Dolag, K., Moscardini, L., Biviano, A., & D'Onofrio, M. 2018, *arXiv:1810.08212*
- Remazeilles, M., Aghanim, N., & Douspis, M. 2013, *MNRAS*, 430, 370
- Ricker, P. M., & Sarazin, C. L. 2001, *ApJ*, 561, 621
- Roettiger, K., Burns, J. O., & Stone, J. M. 1999, *ApJ*, 518, 603
- Ruggiero, R., & Lima Neto, G. B. 2017, *MNRAS*, 468, 4107
- Russell, H. R., van Weeren, R. J., Edge, A. C., et al. 2011, *MNRAS*, 417, L1
- Russell, H. R., McNamara, B. R., Sanders, J. S., et al. 2012, *MNRAS*, 423, 236
- Rykoff, E. S., Evrard, A. E., McKay, T. A., et al. 2008, *MNRAS*, 387, L28
- Sarazin, C. L. 2002, in *Astrophysics and Space Science Library*, Vol. 272, *Merging Processes in Galaxy Clusters*, ed. L. Feretti, I. M. Gioia, & G. Giovannini, 1–38

- Sarazin, C. L., Finoguenov, A., Wik, D. R., & Clarke, T. E. 2016, ArXiv:160607433
- Schneider, P., van Waerbeke, L., Jain, B., & Kruse, G. 1998, MNRAS, 296, 873
- Shaw, L. D., Holder, G. P., & Bode, P. 2008, ApJ, 686, 206
- Shimwell, T. W., Röttgering, H. J. A., Best, P. N., et al. 2017, A&A, 598, A104
- Shimwell, T. W., Tasse, C., Hardcastle, M. J., et al. 2018, ArXiv e-prints
- Stroe, A., Sobral, D., Paulino-Afonso, A., et al. 2017, MNRAS, 465, 2916
- Stroe, A., Sobral, D., Dawson, W., et al. 2015, MNRAS, 450, 646
- Takizawa, M., & Naito, T. 2000, ApJ, 535, 586
- Tanaka, M., Coupon, J., Hsieh, B.-C., et al. 2018, PASJ, 70, S9
- Taylor, J. E., & Babul, A. 2005, MNRAS, 364, 515
- Thompson, R., & Nagamine, K. 2012, MNRAS, 419, 3560
- Tinker, J., Kravtsov, A. V., Klypin, A., et al. 2008, ApJ, 688, 709
- Tormen, G., Moscardini, L., & Yoshida, N. 2004, MNRAS, 350, 1397
- Truemper, J. 1982, Advances in Space Research, 2, 241
- Umetsu, K., Medezinski, E., Nonino, M., et al. 2014, ApJ, 795, 163
- van Weeren, R. J., Brügger, M., Röttgering, H. J. A., et al. 2011, A&A, 533, A35
- van Weeren, R. J., Röttgering, H. J. A., Brügger, M., & Hoeft, M. 2010, Science, 330, 347
- van Weeren, R. J., Andrade-Santos, F., Dawson, W. A., et al. 2017, Nature Astronomy, 1, 0005
- Venturi, T., Giacintucci, S., Brunetti, G., et al. 2007, A&A, 463, 937
- Venturi, T., Giacintucci, S., Dallacasa, D., et al. 2008, A&A, 484, 327
- Vikhlinin, A., Burenin, R. A., Ebeling, H., et al. 2009, ApJ, 692, 1033
- Wen, Z. L., Han, J. L., & Liu, F. S. 2012, ApJS, 199, 34
- Yang, X., Mo, H. J., van den Bosch, F. C., et al. 2006, MNRAS, 373, 1159
- Yu, L., Nelson, K., & Nagai, D. 2015, ApJ, 807, 12
- ZuHone, J. A. 2011, ApJ, 728, 54